10 Flaw Scattering

Ultrasonic beam models can simulate the fields incident on a flaw in an ultrasonic inspection. Given those incident fields, we then must also determine the scattered waves produced by the interactions of those fields with the flaw. For complex flaw morphologies numerical methods are generally needed to solve for these scattered waves. For a number of simple flaw shapes and types, however, we can model some important characteristics of the flaw scattering process explicitly with approximate methods. In this Chapter we will describe two such approximations – the Kirchhoff approximation and the Born approximation – and also give a brief overview of a number of other flaw scattering methods.

10.1 The Far-Field Scattering Amplitude

To describe flaw scattering we will first consider the simple case shown in Fig. 10.1 where a plane wave in a fluid strikes an immersed object, generating scattered waves that travel from the "flaw" in all directions. At a distance of many wavelengths from the flaw, the flaw acts like a point source generating a spherical wave, as shown in Fig. 10.1. We can express the pressure in this spherical wave as

$$p^{scatt}\left(\mathbf{y},\omega\right) = p_0 A\left(\mathbf{e}_i;\mathbf{e}_s\right)\frac{\exp\left(ik_p r_s\right)}{r_s}, \tag{10.1}$$

where p_0 is the pressure amplitude of the incident wave, $A\left(\mathbf{e}_i;\mathbf{e}_s\right)$ is the *far-field scattering amplitude* of the flaw in the $\mathbf{e}_s$ direction due to an incident wave traveling in the $\mathbf{e}_i$ direction. The scattering amplitude is also a function of frequency but for economy of notation we will not show this frequency dependence explicitly. Note that we have implicitly assumed harmonic waves of $\exp\left(-i\omega t\right)$ time dependency, a factor that also will not be shown explicitly. The variable r_s is the distance from a

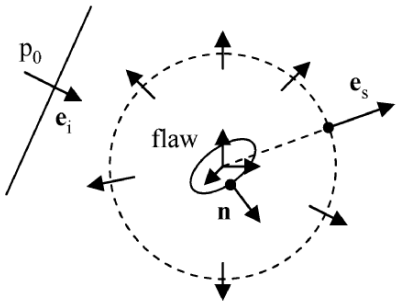

Fig. 10.1. The spherical P-wave scattered in the far-field from a "flaw" in a fluid due to an incident wave of pressure amplitude p_0.

fixed point at the flaw (usually taken to be the flaw "center") to the point in the fluid where the scattered pressure is being determined, and k_p is the wave number for compressional waves in the fluid.

It can be shown that the far-field scattering amplitude is related to the total fields (incident plus scattered fields) on the surface of the flaw through a surface integral given by [Fundamentals]:

$$A(\mathbf{e}_i;\mathbf{e}_s)=\frac{-1}{4\pi}\int_{S_f}\left[\frac{\partial\tilde{p}}{\partial n}+ik_p(\mathbf{e}_s\cdot\mathbf{n})\tilde{p}\right]\exp\left(-ik_p\mathbf{x}_s\cdot\mathbf{e}_s\right)dS(\mathbf{x}_s), \qquad (10.2)$$

where **n** is the unit outwards normal to the surface of the flaw pointing into the fluid, $\mathbf{x}_s$ is a general point on the surface, S_f, and $\tilde{p}=p(\mathbf{x}_s,\omega)/p_0$ is the pressure normalized by the incident wave pressure amplitude. Note that the far-field scattering amplitude as defined here has a dimension of length. The unit vector $\mathbf{e}_i$ does not appear explicitly in Eq. (10.2) but the fields do depend on this direction so it is included as an argument of the scattering amplitude. Since $\partial p/\partial n=i\omega\rho v_n$ from the equation of motion for the fluid the scattering amplitude depends on both the pressure, *p*, and the normal component of the velocity, v_n, on the surface. It is possible to specify one of these variables. For example, for a void, we can set $p=0$, while for a rigid, immobile scatterer we would have $v_n=0$. For an elastic inclusion, we would have to instead specify conditions of continuity of the tractions and normal velocity at the surface. Given the incident waves and a set of boundary conditions of one of these types, it is then possible

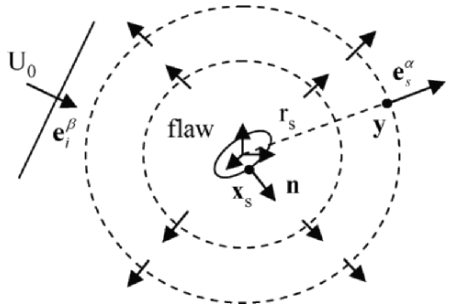

Fig. 10.2. The spherical P- and S-waves scattered in the far-field from a flaw in an elastic solid due to an incident wave of displacement amplitude U_0.

to formulate a boundary value problem and solve for the unknown fields on the surface of the scatterer [Fundamentals].

For ultrasonic NDE inspection problems the flaws of interest are located in an elastic solid. The scattering of elastic waves is more complex than the fluid case just considered, but again at a distance of many wavelengths from the flaw the scattered waves are just spherical waves, as shown in Fig. 10.2. In this case a flaw generates both scattered spherical P-waves and S-waves. The displacement of the solid produced by these scattered waves can be written as

$$\mathbf{u}^{scatt}\left(\mathbf{y},\omega\right)=U_0\mathbf{A}\left(\mathbf{e}_i^{\beta};\mathbf{e}_s^{p}\right)\frac{\exp\left(ik_p r_s\right)}{r_s}+U_0\mathbf{A}\left(\mathbf{e}_i^{\beta};\mathbf{e}_s^{s}\right)\frac{\exp\left(ik_s r_s\right)}{r_s}, \qquad (10.3)$$

where U_0 is the displacement amplitude of the incident wave, $k_\alpha\ (\alpha=p,s)$ are the wave numbers for P- and S-waves, and $\mathbf{A}\left(\mathbf{e}_i^{\beta};\mathbf{e}_s^{\alpha}\right)$ is the *vector far-field scattering amplitude* for a scattered wave of type α $(\alpha=p,s)$ due to an incident wave of type β $(\beta=p,s)$. The vectors $\mathbf{e}_i^{\beta}$ and $\mathbf{e}_s^{\alpha}$ are unit vectors in the incident and scattered wave directions, respectively [Note: lower case p and s superscripts will be used here to denote P-waves and S-waves, respectively, while an s subscript will denote a "scattered" wave unit vector]. Far-field scattering amplitudes for both P-waves and S-waves can be written in terms of a single vector-valued function, $\mathbf{f}^{\alpha;\beta}$, where [Fundamentals]:

$$\begin{aligned}\mathbf{f}^{\alpha;\beta} &= f_l^{\alpha;\beta}\mathbf{i}_l \\ &= -\frac{\mathbf{i}_l}{4\pi\rho c_\alpha^2}\int_S \left[\tilde{\tau}_{lk}n_k + ik_\alpha C_{lkpj}e_{sk}^\alpha n_p \tilde{u}_j\right] \\ &\cdot\exp\left(-ik_\alpha \mathbf{x}_s\cdot\mathbf{e}_s^\alpha\right)dS\left(\mathbf{x}_s\right)\end{aligned} \qquad \text{(no sum on } s\text{)} \quad (10.4)$$

and the vector far-field scattering amplitudes for P-waves and S-waves are given by

$$\begin{aligned}\mathbf{A}\left(\mathbf{e}_i^\beta;\mathbf{e}_s^p\right) &= \left(\mathbf{f}^{p;\beta}\cdot\mathbf{e}_s^p\right)\mathbf{e}_s^p \\ \mathbf{A}\left(\mathbf{e}_i^\beta;\mathbf{e}_s^s\right) &= \left[\mathbf{f}^{s;\beta} - \left(\mathbf{f}^{s;\beta}\cdot\mathbf{e}_s^s\right)\mathbf{e}_s^s\right]\end{aligned} \qquad \text{(no sum on } s\text{)} \quad (10.5)$$

for $\beta = (p,s)$. The vectors $\mathbf{i}_l$ are unit vectors along a set of Cartesian coordinate axes. The n_k terms in Eq. (10.4) are the components of the unit outward normal to the flaw surface (see Fig. 10.2) and C_{ijkl} is the fourth order elastic constants tensor, which here is taken to be for an isotropic elastic material. The stress and displacement components in Eq. (10.4) are normalized by the displacement amplitude of the incident wave, i.e. $\tilde{\tau}_{ij} = \tau_{ij}/U_0, \tilde{u}_j = u_j/U_0$. From Eq. (10.5) it can be seen that the polarization of the scattered P-wave is in the $\mathbf{e}_s^p$ direction while the polarization of the scattered S-wave is perpendicular to the $\mathbf{e}_s^s$ direction since $\mathbf{A}\left(\mathbf{e}_i^\beta;\mathbf{e}_s^s\right)\cdot\mathbf{e}_s^s = 0$.

In an ultrasonic flaw measurement system the output is a voltage which is a scalar quantity. Thus, if the scattering amplitude appears explicitly as part of a model for this measured voltage – which it does under certain conditions, as discussed in the next Chapter – there must be a specific scalar function of the vector scattering amplitude that is related to the output voltage. In the next Chapter it will be shown that the appropriate scalar function that appears in a model of the entire ultrasonic measurement system is the scalar component

$$A\left(\mathbf{e}_i^\beta;\mathbf{e}_s^\alpha\right) = \mathbf{A}\left(\mathbf{e}_i^\beta;\mathbf{e}_s^\alpha\right)\cdot\left(-\mathbf{d}^\alpha\right). \quad (10.6)$$

The unit vector $\mathbf{d}^\alpha$ is the polarization vector of a wave of type α (the same type as the scattered wave) that travels from the receiving transducer (acting like a transmitter) to the flaw along a completely reversed path from the path that the scattered waves take from the flaw to the receiving transducer (see Fig. 10.3). This polarization vector is defined when one

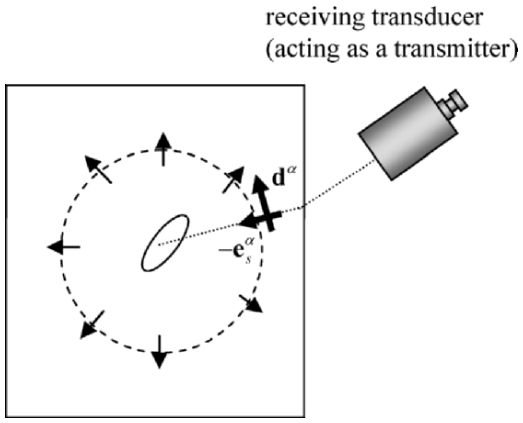

Fig. 10.3. The polarization, $\mathbf{d}^\alpha$, of the wave traveling from the receiver (acting as a transmitter) to the flaw along a path that is completely reversed from the actual received wave traveling from the flaw to the receiving transducer. For a scattered P-wave (α = p) we have $\mathbf{d}^\alpha = -\mathbf{e}_s^\alpha$ while for a scattered S-wave $\mathbf{d}^\alpha$ is perpendicular to $\mathbf{e}_s$.

solves for the waves propagated from the receiving transducer to the flaw. Note that the choice of sign of the polarization vector is arbitrary. For example, for a plane P-wave traveling in the **e**-direction with velocity given by $\mathbf{v} = V\mathbf{e}$, we could take the polarization $\mathbf{d}^p = \mathbf{e}$ (as is normally done) and write $\mathbf{v} = V\mathbf{d}^p$ or we could choose $\mathbf{d}^p = -\mathbf{e}$ and write $\mathbf{v} = -V\mathbf{d}^p$ instead. The velocity of the wave is unaffected by this choice. Choosing a different sign on the polarization vector will affect the sign of the amplitude, as shown by this simple example, or it can affect individual parts of the total expression for the wave field such as transmission or reflection coefficients since those coefficients depend on the choice of the polarization direction (see Appendix D where the transmission coefficients were defined for specific choices of P-wave and S-wave polarizations). Sign changes of the transmission/reflection coefficients and polarizations, however, cancel so again the total wave field is unaffected by the choice for the direction of the polarization. However, with a given choice of the polarization vector we must be careful to use the transmission/reflection coefficients consistent with that choice.

Using Eqs. (10.4) and (10.5) in Eq. (10.6), the scalar scattering component, $A\left(\mathbf{e}_i^\beta; \mathbf{e}_s^\alpha\right)$ for both P-waves and S-waves is given by

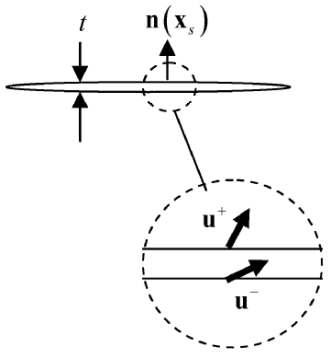

Fig. 10.4. A crack modeled as an open surface in a solid that is obtained by letting the thickness, *t*, go to zero of a thin volumetric shape, as shown, where the stress vector is zero on both sides of the crack but the displacement vector is allowed to have a displacement discontinuity given by $\Delta u(\mathbf{x}_s,\omega)=\mathbf{u}^+-\mathbf{u}^-$, where $\mathbf{u}^+,\mathbf{u}^-$ are displacements on opposite sides of the crack at the same location on the open surface.

$$A(\mathbf{e}_i^\beta;\mathbf{e}_s^\alpha)=\frac{1}{4\pi\rho c_\alpha^2}\int_S d_l^\alpha\left[\tilde{\tau}_{lk}n_k+ik_\alpha C_{lkpj}e_{sk}^\alpha n_p\tilde{u}_j\right]\cdot\exp\left(-ik_\alpha\mathbf{x}_s\cdot\mathbf{e}_s^\alpha\right)dS(\mathbf{x}_s). \quad \text{(no sum on } s,\ \alpha) \tag{10.7}$$

Equation (10.7) gives the far-field scalar scattering response of a general volumetric flaw. One can also use this result and a limiting argument to obtain the response of a crack-like flaw where the crack is modeled as a zero volume open surface (Fig. 10.4). If one assumes that the faces of the crack are stress-free, we have on both faces of the crack $\tilde{\tau}_{lk}n_k=0$. The displacement components, however, can be different from one face of the crack to the other, leading to *displacement discontinuities*, $\Delta\tilde{u}_j(\mathbf{x}_s,\omega)$, on the crack (see Fig. 10.4). The scattering amplitude of Eq. (10.7) then reduces to [Fundamentals]

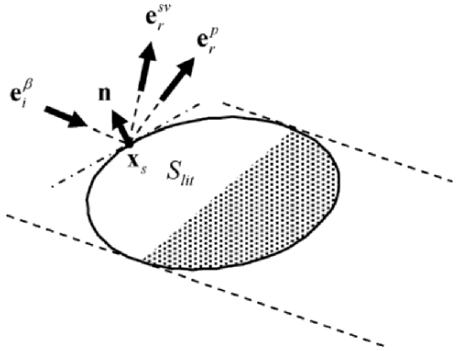

Fig. 10.5. The Kirchhoff approximation, where the fields on the "lit" surface of the flaw are assumed to be those obtained by plane wave interactions with a plane (dashed-dotted line) whose normal coincides with that of the flaw surface. On the remainder of the flaw surface (the shaded "shadow" region shown) the fields are assumed to be identically zero.

$$A\left(\mathbf{e}_i^{\beta};\mathbf{e}_s^{\alpha}\right)=\frac{1}{4\pi\rho c_{\alpha}^2}\int_S\left[ik_{\alpha}C_{lkpj}d_l^{\alpha}e_{sk}^{\alpha}n_p\Delta\tilde{u}_j\right]\cdot\exp\left(-ik_{\alpha}\mathbf{x}_s\cdot\mathbf{e}_s^{\alpha}\right)dS\left(\mathbf{x}_s\right), \quad \text{(no sum on } s,\ \alpha\text{)} \tag{10.8}$$

where now S is the (open) surface of the crack and **n** is the unit normal to that open surface.

10.2 The Kirchhoff Approximation for Volumetric Flaws

One approximation that has been frequently used to describe the scattering of volumetric flaws or cracks is the Kirchhoff approximation [Fundamentals]. Consider first the volumetric flaw case. In this approximation, that part of the flaw surface where the incident wave (which is taken as a plane wave) can directly strike the surface is called the "lit" surface, S_{lit} (Fig. 10.5). On the lit surface it is assumed that the interaction of the incident plane wave with the surface is identical to that of the incident wave with a plane interface whose normal coincides locally with the surface normal, **n**. Since we can solve for the interaction of a plane wave with a plane interface, we can write down explicit expressions for

both the Kirchhoff approximation displacement components, $\tilde{u}_j^K$, and stresses, $\tilde{\tau}_{lk}^K$, on the lit surface as [Fundamentals]

$$\begin{aligned}\tilde{u}_j^K &= d_{ij}^{\beta}\exp\left[ik_{\beta}\left(\mathbf{e}_i^{\beta}\cdot\mathbf{x}_s\right)\right]+\sum_{m=p,sv}R_{12}^{m;\beta}d_{rj}^{m}\exp\left[ik_m\left(\mathbf{e}_r^{m}\cdot\mathbf{x}_s\right)\right]\\ \tilde{\tau}_{lk}^K &= C_{lkjp}\partial\tilde{u}_j^K/\partial x_p,\end{aligned} \qquad (10.9)$$

(no sum on r,i)

where $\mathbf{d}_i^{\beta}$ is the polarization vector for an incident wave (of type β) traveling in the $\mathbf{e}_i^{\beta}$ direction and $\mathbf{d}_r^{m}$ is the polarization of a reflected waves at the interface (of type m) traveling in the $\mathbf{e}_r^{m}$ direction. The reflection coefficients for a reflected wave of type m due to an incident wave of type β are the $R_{12}^{m;\beta}$. On the remaining part of the flaw surface where the incident wave cannot strike it directly, it assumed that the fields are totally absent and $\tilde{u}_j=\tilde{\tau}_{lk}=0$. Then Eq. (10.7) becomes

$$\begin{aligned}A\left(\mathbf{e}_i^{\beta};\mathbf{e}_s^{\alpha}\right)=\frac{1}{4\pi\rho c_{\alpha}^2}\int_{S_{lit}} & d_l^{\alpha}\left[\tilde{\tau}_{lk}^K n_k+ik_{\alpha}C_{lkpj}e_{sk}^{\alpha}n_p\tilde{u}_j^K\right]\\ &\cdot\exp\left(-ik_{\alpha}\mathbf{x}_s\cdot\mathbf{e}_s^{\alpha}\right)dS\left(\mathbf{x}_s\right).\end{aligned} \qquad (10.10)$$

(no sum on s, α)

The Kirchhoff approximation is a high frequency approximation that allows us to avoid having to solve a boundary value problem in order to determine the far-field scattering amplitude. In general, the integrations in Eq. (10.10) must still be done numerically, but for the special case of the pulse-echo response of a void one can obtain some simple and explicit results. In that case we consider a scattered wave of the same type as the incident wave and let the scattered wave direction be opposite to that of the incident wave so that $\mathbf{e}_s^{\alpha}=-\mathbf{e}_i^{\beta}$. Since we are considering a void we also have $\tilde{\tau}_{lk}n_k=0$ on the surface. Then Eq. (10.10) reduces to

$$A\left(\mathbf{e}_i^{\beta};-\mathbf{e}_i^{\beta}\right)=\frac{1}{4\pi\rho c_{\beta}^2}\int_{S_{lit}}\left[-ik_{\beta}C_{lkpj}d_l^{\beta}e_{ik}^{\beta}n_p\tilde{u}_j^K\right]\exp\left(ik_{\beta}\mathbf{x}_s\cdot\mathbf{e}_i^{\beta}\right)dS\left(\mathbf{x}_s\right). \qquad (10.11)$$

(no sum on s, β)

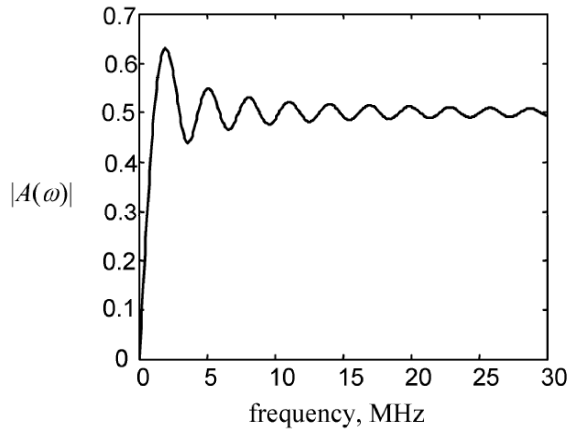

Fig. 10.6. Magnitude of the far-field pulse-echo P-wave scattering amplitude versus frequency for a 1 mm radius void in steel ($c_p = 5900$ m/s) in the Kirchhoff approximation.

Equation (10.11) can be simplified even further since it can be shown by a combination of analytical and numerical evaluations that [10.1]

$$\frac{C_{lkpj} d_l^{\beta} e_{ik}^{\beta} n_p u_j^K}{\rho c_{\beta}^2} = 2\left(\mathbf{e}_i^{\beta} \cdot \mathbf{n}\right) \exp\left[ik_{\beta} \left(\mathbf{e}_i^{\beta} \cdot \mathbf{x}_s\right)\right] \tag{10.12}$$

and the pulse-echo far-field scattering amplitude of the void becomes simply

$$A\left(\mathbf{e}_i^{\beta}; -\mathbf{e}_i^{\beta}\right) = \frac{-ik_{\beta}}{2\pi} \int_{S_{III}} \left(\mathbf{e}_i^{\beta} \cdot \mathbf{n}\right) \exp\left(2ik_{\beta} \mathbf{x}_s \cdot \mathbf{e}_i^{\beta}\right) dS\left(\mathbf{x}_s\right). \tag{10.13}$$

Equation (10.13) is identical to the pulse-echo response of a void using a fluid model (see Eq. (10.2)) instead [Fundamentals]. It is a very important result since it shows that:

For any stress-free flaw in an isotropic elastic solid the Kirchhoff approximation for the pulse-echo far-field scattering amplitude component that appears in an ultrasonic measurement model is identical to the Kirchhoff approximation for the scalar scattering amplitude of a void in a fluid.

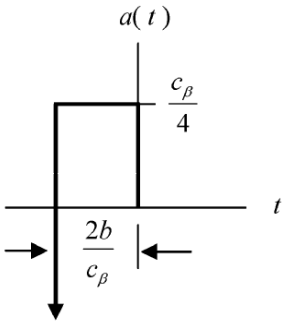

Fig. 10.7. The time domain pulse-echo impulse response of a spherical void in a solid in the Kirchhoff approximation, showing the leading edge delta function response followed by the response of the lit surface.

In this Chapter we will use this result to carry out the integrations in Eq. (10.13) explicitly for a number of important canonical scattering geometries including a spherical void, a flat elliptical crack (see Eq. (10.32)), and a side-drilled hole (see Eq. (10.53)). For a spherical void of radius *b*, for example, Eq. (10.13) gives [Fundamentals]

$$A\left(\mathbf{e}_i^\beta;-\mathbf{e}_i^\beta\right)=\frac{-b}{2}\exp\left(-ik_\beta b\right)\left[\exp\left(-ik_\beta b\right)-\frac{\sin\left(k_\beta b\right)}{k_\beta b}\right]. \tag{10.14}$$

Figure 10.6 plots the magnitude of this scattering amplitude for a spherical void in steel. The characteristics of this plot can be better understood if we Fourier transform Eq. (10.14) into the time domain. This leads to the impulse response of the flaw, $a\left(\mathbf{e}_i^\beta;\mathbf{e}_s^\alpha,t\right)$, given by [Fundamentals]

$$a\left(\mathbf{e}_i^\beta;-\mathbf{e}_i^\beta,t\right)=\frac{-b}{2}\left[\delta\left(t+\frac{2b}{c_\beta}\right)-\frac{c_\beta}{2b}U\left(\frac{-2b}{c_\beta},0;t\right)\right], \tag{10.15}$$

where δ is a delta function (see Appendix A) and

$$U\left(t_1,t_2;t\right)=\begin{cases}1 & t_1<t<t_2\\ 0 & otherwise\end{cases}. \tag{10.16}$$

Figure 10.7 shows a plot of this time domain scattering amplitude. When the incident wave first reaches the flaw, there is a delta function response from the point where the incident wave first touches the flaw. This *leading*

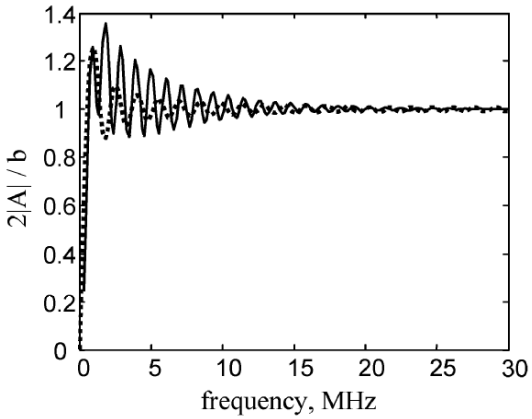

Fig. 10.8. The magnitude of the normalized scattering amplitude versus frequency for the pulse-echo P-wave response of a spherical void in the the Kirchhoff approximation (dotted line) and for the exact separation of variables solution (solid line).

edge response occurs at time $t = -2b/c_\beta$, where $t = 0$ is when the wave front reaches the center of the flaw, followed by a constant response that exists as the wave front sweeps across the lit surface. When the wave front reaches the boundary between the lit surface and the shadow zone of the flaw the response drops to zero. It is the interference of the leading edge response and the remaining lit surface response that causes the oscillations seen in Fig. 10.6. At very high frequencies, only the leading edge response remains, leading to the plateau seen in Fig. 10.6.

The sphere is one of the few shapes where we can obtain the exact far-field scattering amplitude by the method of separation of variables [Fundamentals]. Thus, we can compare the Kirchhoff approximation to the exact results for the spherical void just considered. Figure 10.8 shows this comparison made in the frequency domain for the normalized magnitude of the far-field scattering amplitude computed for the pulse-echo P-wave response of a spherical void. The two results agree at high frequencies, which show that the leading edge delta function response in the Kirchhoff approximation agrees with this same response in the exact solution. The frequency of oscillations in the exact solution is different from that in the Kirchhoff approximation because in the exact solution the oscillations are caused primarily by an interference of the leading edge response with a *creeping wave* that travels around the flaw and returns, as shown schematically in Fig. 10.9. This creeping wave can be seen explicitly in

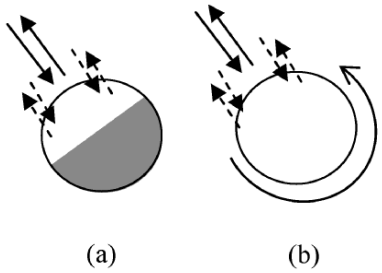

Fig. 10.9. The scattering from a spherical void in **(a)** the Kirchhoff approximation, where the response comes from a front surface leading edge response (solid arrows) and the response from the lit surface (dashed arrows), and in **(b)** the exact solution case where there are contributions from the leading edge and front surface but where there also exists a creeping wave that travels around the sphere as shown.

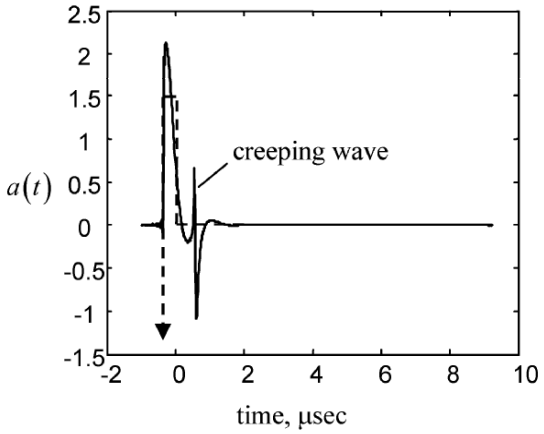

Fig. 10.10. The exact time domain pulse-echo impulse response (solid line) of a 1 mm radius spherical void in a solid as calculated from a separation of variables solution with the delta function removed, showing the response from the lit surface and a creeping wave. The same response in the Kirchhoff approximation (dashed line). Wave speeds: c_p = 6000 m/sec, c_s = 3200 m/sec.

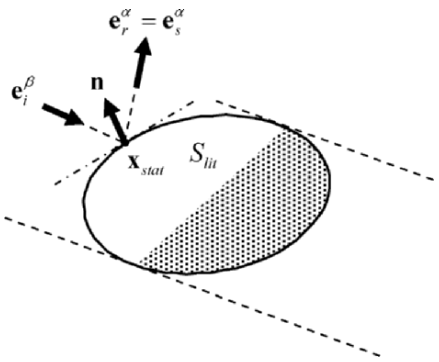

Fig. 10.11. The case where a stationary phase point, $\mathbf{x}_{stat}$, exists on the lit surface of a flaw, where the scattered wave direction coincides with one of the reflected wave directions.

Fig. 10.10 which shows the exact P-wave pulse-echo time domain impulse response of the spherical void obtained by Fourier transforming the exact separation of variables solution (after removal of the delta function leading edge response which is common to both the exact solution and the Kirchhoff approximation). The Kirchhoff solution is also shown in Fig. 10.10 for comparison purposes.

10.3 The Leading Edge Response of Volumetric Flaws

Although as we have seen the Kirchhoff approximation did not accurately represent the later arriving waves from a spherical void, it did model correctly the leading edge response of the flaw. This leading response is the dominant part of the solution at high frequencies, and in the time domain gives us a delta function signal from the front surface of the flaw. Since the delta function contains all frequencies equally whereas other parts of the flaw response typically go to zero as the frequency increases, even in real band-limited systems the leading edge response signal in the time domain is often the largest signal in the entire flaw response. Thus, it is useful to try to model this signal by itself. Fortunately, this is possible for general volumetric flaw types, not just voids. If we return to the Kirchhoff approximation (Eq. (10.10)) for a general volumetric flaw, we can approximate the integral in that equation at high frequencies by the method of stationary phase. The details are rather lengthy, but the end result is that in a general pitch-catch setup (which includes pulse-echo as a

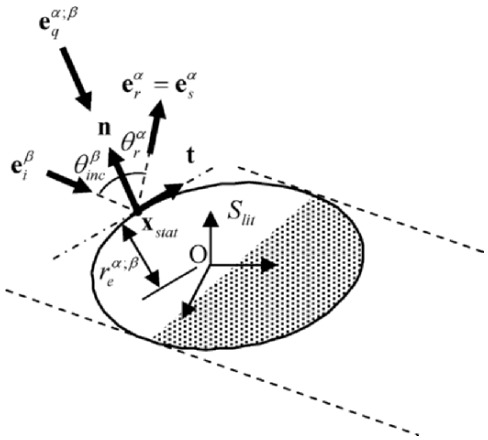

Fig. 10.12. The case where a stationary phase point, $\mathbf{x}_{stat}$, exists on the lit surface of a flaw, where the scattered wave direction coincides with one of the reflected wave directions.

special case) the major contribution to the integral for a scattered wave of type α traveling in the $\mathbf{e}_s^{\alpha}$ direction comes from a neighborhood of a point on the flaw surface, called a stationary phase point, $\mathbf{x}_{stat}$, where the direction of the reflected wave in the Kirchhoff approximation, $\mathbf{e}_r^{\alpha}$, coincides with $\mathbf{e}_s^{\alpha}$ (see Fig. 10.11). The contribution to the integral near this stationary phase point can then be calculated by the method of stationary phase to give, in the frequency domain [Fundamentals]

$$A\left(\mathbf{e}_i^{\beta};\mathbf{e}_s^{\alpha}\right) = \frac{\left(\mathbf{e}_s^{\alpha}\cdot\mathbf{n}\right)R_{12}^{\alpha;\beta}\sqrt{R_1R_2}\left(\mathbf{d}_r^{\alpha}\cdot\mathbf{d}^{\alpha}\right)}{\left|\mathbf{g}^{\alpha;\beta}\cdot\mathbf{n}\right|}\exp\left(ik_{\alpha}\mathbf{g}^{\alpha;\beta}\cdot\mathbf{x}_{stat}\right), \qquad (10.17)$$

where $R_{12}^{\alpha;\beta}$ is the plane wave reflection coefficient (based on velocity ratios) between material 1 (the host material around the flaw) and material 2 (the flaw) for a reflected wave of type α due to an incident wave of type β. R_1, R_2 are the magnitudes of the principal curvatures of the flaw surface at the stationary phase point, $\mathbf{d}_r^{\alpha}$ is the polarization of the reflected wave and $\mathbf{d}^{\alpha}$ is the polarization of the wave coming from the receiving transducer (acting as a transmitter). The vectors $\mathbf{g}^{\alpha;\beta}$ are given by

$$\mathbf{g}^{\alpha;\beta} = \left(c_\alpha / c_\beta\right)\mathbf{e}_i^\beta - \mathbf{e}_s^\alpha, \tag{10.18}$$

where $\mathbf{e}_i^\beta$ is the incident wave direction for a wave of type β, $\mathbf{e}_s^\alpha = \mathbf{e}_r^\alpha$ is the reflected wave direction for a wave of type α, and c_p, c_s are the compressional and shear wave speeds for the host material surrounding the flaw, respectively. Note that one can always define the reflection coefficient so that the reflected wave polarization, $\mathbf{d}_r^\alpha$, coincides with the polarization $\mathbf{d}^\alpha$. In that case we have $\mathbf{d}_r^\alpha \cdot \mathbf{d}^\alpha = 1$. In all the subsequent results we will assume that this is true.

The vectors $\mathbf{g}^{\alpha;\beta}$ can be written in terms of their magnitudes and a unit vector, $\mathbf{e}_q^{\alpha;\beta}$ as $\mathbf{g}^{\alpha;\beta} = \left|\mathbf{g}^{\alpha;\beta}\right|\mathbf{e}_q^{\alpha;\beta}$. At the stationary phase point the unit vector $\mathbf{e}_q^{\alpha;\beta} = -\mathbf{n}$ so that $\left|\mathbf{g}^{\alpha;\beta} \cdot \mathbf{n}\right| = \left|\mathbf{g}^{\alpha;\beta}\right|$. We also have $\mathbf{g}^{\alpha;\beta} \cdot \mathbf{t} = 0$, where $\mathbf{t}$ is a unit vector in the tangent plane to the surface at the stationary phase point (see Fig. 10.12), which is just a statement of Snell's law. We can write the quantity $\mathbf{g}^{\alpha;\beta} \cdot \mathbf{x}_{stat} = -\left|\mathbf{g}^{\alpha;\beta}\right| r_e^{\alpha;\beta}$, where $r_e^{\alpha;\beta}$ is the distance in the direction $\mathbf{n}$ (or, equivalently, $-\mathbf{e}_q^{\alpha;\beta}$) at the stationary phase point from a fixed point (usually taken as the flaw "center") to the tangent plane of the surface at $\mathbf{n}$ (Fig. 10.12). The $r_e^{\alpha;\beta}$ distance is called the *equivalent radius* of the flaw in the $\mathbf{e}_q^{\alpha;\beta}$ direction. Thus, we can also write Eq. (10.17) in the form

$$A\left(\mathbf{e}_i^\beta; \mathbf{e}_s^\alpha\right) = \frac{\left(\mathbf{e}_s^\alpha \cdot \mathbf{n}\right) R_{12}^{\alpha;\beta} \sqrt{R_1 R_2}}{\left|\mathbf{g}^{\alpha;\beta}\right|} \exp\left(-ik_\alpha \left|\mathbf{g}^{\alpha;\beta}\right| r_e^{\alpha;\beta}\right). \tag{10.19}$$

If we Fourier transform Eq. (10.19) into the time domain, the leading edge impulse response of the flaw is given by

$$a\left(\mathbf{e}_i^\beta; \mathbf{e}_s^\alpha, t\right) = \frac{\left(\mathbf{e}_s^\alpha \cdot \mathbf{n}\right) R_{12}^{\alpha;\beta} \sqrt{R_1 R_2}}{\left|\mathbf{g}^{\alpha;\beta}\right|} \delta\left(t + \left|\mathbf{g}^{\alpha;\beta}\right| r_e^{\alpha;\beta} / c_\alpha\right). \tag{10.20}$$

For the special case of a pulse-echo (same mode) leading edge response, from Eqs. (10.19), (10.20) we have the even simpler expressions:

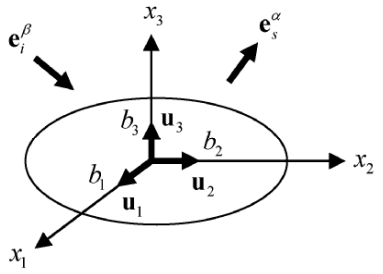

Fig. 10.13. Scattering geometry for an ellipsoidal flaw.

$$A\left(\mathbf{e}_i^\beta;-\mathbf{e}_i^\beta\right)=\frac{R_{12}^{\beta;\beta}\left(0^\circ\right)\sqrt{R_1R_2}}{2}\exp\left(-2ik_\beta r_e\right)$$
$$a\left(\mathbf{e}_i^\beta;-\mathbf{e}_i^\beta,t\right)=\frac{R_{12}^{\beta;\beta}\left(0^\circ\right)\sqrt{R_1R_2}}{2}\delta\left(t+2r_e/c_\beta\right), \tag{10.21}$$

where $r_e=r_e^{\beta;\beta}$ and now the reflection coefficient is just the normal incidence coefficient, as indicated in Eq. (10.21).

For a purely convex flaw shape such as an ellipsoid, as shown in Fig. 10.13, there can be at most only one stationary phase point on the lit surface. However, a stationary point may not exist on the lit surface at all for some combination of incident and scattered directions of a general pitch-catch setup. In that case, a leading edge response of the flaw is absent. For more general flaw shapes there may be multiple stationary phase points, in which case one must sum over all the leading edge responses.

For an ellipsoidal shaped flaw with semi-major axes $\left(b_1,b_2,b_3\right)$ along the $\left(\mathbf{u}_1,\mathbf{u}_2,\mathbf{u}_3\right)$ directions as shown in Fig. (10.13) we have the Gaussian curvature term [Fundamentals]

$$\sqrt{R_1R_2}=b_1b_2b_3/\left(r_e^{\alpha;\beta}\right)^2 \tag{10.22}$$

and the equivalent radius is given by

$$r_e^{\alpha;\beta}=\sqrt{b_1^2\left(\mathbf{e}_q^{\alpha;\beta}\cdot\mathbf{u}_1\right)^2+b_2^2\left(\mathbf{e}_q^{\alpha;\beta}\cdot\mathbf{u}_2\right)^2+b_3^2\left(\mathbf{e}_q^{\alpha;\beta}\cdot\mathbf{u}_3\right)^2}, \tag{10.23}$$

where, recall, $\mathbf{e}_q^{\alpha;\beta}=\mathbf{g}^{\alpha;\beta}/\left|\mathbf{g}^{\alpha;\beta}\right|$ (see Eq. (10.18)).

In this case the leading edge responses for the general pitch-catch setup (Eqs. (10.19) and (10.20)) become

$$A\left(\mathbf{e}_i^{\beta};\mathbf{e}_s^{\alpha}\right)=\frac{\left(\mathbf{e}_s^{\alpha}\cdot\mathbf{n}\right)R_{12}^{\alpha;\beta}b_1b_2b_3}{\left|\mathbf{g}^{\alpha;\beta}\right|\left(r_e^{\alpha;\beta}\right)^2}\exp\left(-ik_{\alpha}\left|\mathbf{g}^{\alpha;\beta}\right|r_e^{\alpha;\beta}\right)$$
$$a\left(\mathbf{e}_i^{\beta};\mathbf{e}_s^{\alpha},t\right)=\frac{\left(\mathbf{e}_s^{\alpha}\cdot\mathbf{n}\right)R_{12}^{\alpha;\beta}b_1b_2b_3}{\left|\mathbf{g}^{\alpha;\beta}\right|\left(r_e^{\alpha;\beta}\right)^2}\delta\left(t+\left|\mathbf{g}^{\alpha;\beta}\right|r_e^{\alpha;\beta}/c_{\alpha}\right) \tag{10.24}$$

and for the pulse-echo case Eq. (10.21) reduces to

$$A\left(\mathbf{e}_i^{\beta};-\mathbf{e}_i^{\beta}\right)=\frac{R_{12}^{\beta;\beta}\left(0^{\circ}\right)b_1b_2b_3}{2r_e^2}\exp\left(-2ik_{\beta}r_e\right)$$
$$a\left(\mathbf{e}_i^{\beta};-\mathbf{e}_i^{\beta},t\right)=\frac{R_{12}^{\beta;\beta}\left(0^{\circ}\right)b_1b_2b_3}{2r_e^2}\delta\left(t+2r_e/c_{\beta}\right). \tag{10.25}$$

For the particular case of a spherical void we have $b_1=b_2=b_3=b$, $R_{12}^{\beta;\beta}\left(0^{\circ}\right)=-1$, and $r_e=b$ so the pulse-echo results of Eq. (10.25) reduce to the leading edge results obtained previously as part of the full Kirchhoff solution for the sphere (see Eqs. (10.14) and (10.15)).

10.4 The Kirchhoff Approximation for Cracks

Our crack scattering model (Eq. (10.8)) considers the crack as a stress-free open surface on which there is a displacement discontinuity $\Delta\mathbf{u}\left(x_s,\omega\right)=\mathbf{u}^{+}-\mathbf{u}^{-}$. In the Kirchhoff approximation on the lit part of the front surface of the crack we would have $u_j^{+}=u_j^{K}$ and on the remainder of the front surface and the entire back surface (assuming the crack does not fold over so that part of the back surface can also be a "lit" surface) we would have zero displacements. Thus, the Kirchhoff approximation for a crack in an elastic solid gives

$$A\left(\mathbf{e}_i^{\beta};\mathbf{e}_s^{\alpha}\right)=\frac{1}{4\pi\rho c_{\alpha}^2}\int_{S_{lit}}\left[ik_{\alpha}C_{lkpj}d_l^{\alpha}e_{sk}^{\alpha}n_p\tilde{u}_j^{K}\right]\exp\left(-ik_{\alpha}\mathbf{x}_s\cdot\mathbf{e}_s^{\alpha}\right)dS\left(\mathbf{x}_s\right). \tag{10.26}$$

(no sum on s, α)

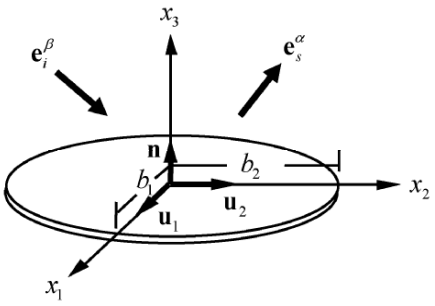

Fig. 10.14. Scattering geometry for a flat elliptical crack.

For the special case of pulse-echo we can again use Eq. (10.12) and write

$$A\left(\mathbf{e}_i^\beta;-\mathbf{e}_i^\beta\right)=\frac{-ik_\beta}{2\pi}\int_{S_{lit}}\left(\mathbf{e}_i^\beta\cdot\mathbf{n}\right)\exp\left(2ik_\beta\mathbf{x}_s\cdot\mathbf{e}_i^\beta\right)dS\left(\mathbf{x}_s\right). \tag{10.27}$$

Thus, the same Kirchhoff approximation expressions we used for the volumetric void can also be used for a crack. The only difference is that in Eqs. (10.26) and (10.27) we are integrating over the lit portion of an open surface of the crack rather than the lit part of a closed surface surrounding a volumetric flaw.

Now, consider the special case when the crack is a flat surface. Then Eq. (10.26) can be written as

$$A\left(\mathbf{e}_i^\beta;\mathbf{e}_s^\alpha\right)=\frac{ik_\alpha C^{\alpha;\beta}}{2\pi}\int_S\exp\left[i\left(k_\beta\mathbf{e}_i^\beta-k_\alpha\mathbf{e}_s^\alpha\right)\cdot\mathbf{x}_s\right]dS\left(\mathbf{x}_s\right), \tag{10.28}$$

where

$$C^{\alpha;\beta}=C_{kplj}e_{sj}^\alpha d_l^\alpha\left(d_{ip}^\beta+\sum_{m=p,s}R_{12}^{m;\beta}d_{rp}^m\right)n_k/2\rho c_\alpha^2 \tag{10.29}$$

In this case the lit surface is now the entire surface, S, of the flaw. For the flat crack in pulse-echo, from Eq. (10.27)

$$A\left(\mathbf{e}_i^\beta;-\mathbf{e}_i^\beta\right)=\frac{-ik_\beta\left(\mathbf{e}_i^\beta\cdot\mathbf{n}\right)}{2\pi}\int_S\exp\left(2ik_\beta\mathbf{x}_s\cdot\mathbf{e}_i^\beta\right)dS\left(\mathbf{x}_s\right). \tag{10.30}$$

For the elliptical flat crack geometry shown in Fig. 10.14, the integrals in Eqs. (10.28) and (10.30) can be performed explicitly. We find for the pitch-catch case [Fundamentals]

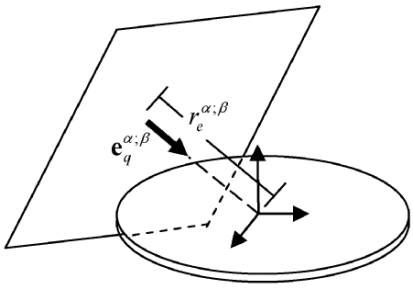

Fig. 10.15. The equivalent radius, $r_e^{\alpha;\beta}$ for the scattering by an elliptical crack shown as the distance from the center of the ellipse to a plane that is normal to $\mathbf{e}_q^{\alpha;\beta}$ and touches the crack edge at a single point.

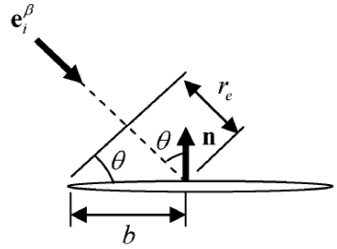

Fig. 10.16. The pulse-echo response of a circular flat crack of radius b showing that the equivalent radius $r_e = b\sin\theta$ where θ is the angle between the incident wave direction and the unit normal to the crack.

$$A\left(\mathbf{e}_i^{\beta};\mathbf{e}_s^{\alpha}\right) = \frac{ib_1b_2C^{\alpha;\beta}}{\left|\mathbf{g}^{\alpha;\beta}\right| r_e^{\alpha;\beta}} J_1\left(k_\alpha \left|\mathbf{g}^{\alpha;\beta}\right| r_e^{\alpha;\beta}\right) \tag{10.31}$$

and for the pulse-echo case

$$A\left(\mathbf{e}_i^{\beta};-\mathbf{e}_i^{\beta}\right) = \frac{-ib_1b_2\left(\mathbf{e}_i^{\beta}\cdot\mathbf{n}\right)}{2r_e} J_1\left(2k_\alpha r_e\right), \tag{10.32}$$

where

$$r_e^{\alpha;\beta} = \sqrt{b_1^2\left(\mathbf{e}_q^{\alpha;\beta}\cdot\mathbf{u}_1\right)^2 + b_2^2\left(\mathbf{e}_q^{\alpha;\beta}\cdot\mathbf{u}_2\right)^2} \tag{10.33}$$

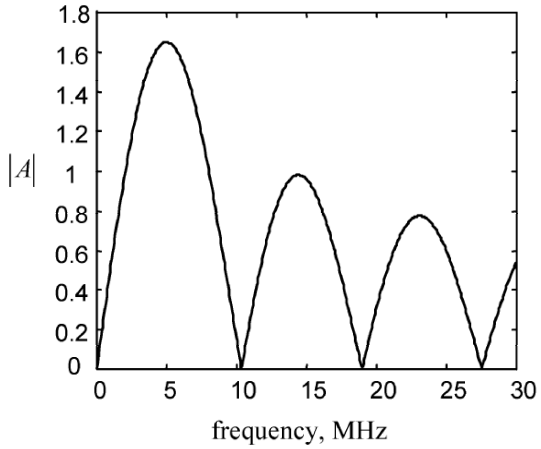

Fig. 10.17. The magnitude of the P-wave pulse-echo far-field scattering amplitude versus frequency calculated in the Kirchhoff approximation for a 1 mm radius circular crack in steel with an angle of incidence of 10° from the crack normal.

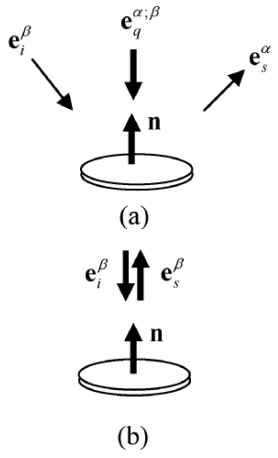

Fig. 10.18. (a) The "generalized normal incidence" case for pitch-catch where $\mathbf{e}_q^{\alpha;\beta}$ is parallel to the crack normal, and **(b)** the pulse-echo case where $\mathbf{e}_i^{\beta} = -\mathbf{e}_s^{\beta}$ is parallel to the normal.

and again we have $\mathbf{e}_q^{\alpha;\beta} = \mathbf{g}^{\alpha;\beta} / \left|\mathbf{g}^{\alpha;\beta}\right|$ (see Eq. (10.18)). For the pulse-echo case we have let $r_e = r_e^{\beta;\beta}$. As in the volumetric flaw case, we can interpret $r_e^{\alpha;\beta}$ as an "equivalent radius" for a given setup, as shown in Fig. 10. 15. In this case the equivalent radius is the distance in the $\mathbf{e}_q^{\alpha;\beta}$ direction from the center of the ellipse to a plane whose normal is $\mathbf{e}_q^{\alpha;\beta}$ and is touching the edge of the crack at a single point.

For the special case of the circular crack $b_1 = b_2 = b$ so that we find in the pitch-catch case

$$A\left(\mathbf{e}_i^{\beta};\mathbf{e}_s^{\alpha}\right) = \frac{ib^2 C^{\alpha;\beta}}{\left|\mathbf{g}^{\alpha;\beta}\right| r_e^{\alpha;\beta}} J_1\left(k_\alpha \left|\mathbf{g}^{\alpha;\beta}\right| r_e^{\alpha;\beta}\right) \tag{10.34}$$

and in the pulse-echo case

$$A\left(\mathbf{e}_i^{\beta};-\mathbf{e}_i^{\beta}\right) = \frac{-ib^2\left(\mathbf{e}_i^{\beta}\cdot\mathbf{n}\right)}{2r_e} J_1\left(2k_\beta r_e\right). \tag{10.35}$$

In the pulse-echo response of the circular crack we have $\mathbf{e}_i \cdot \mathbf{n} = -\cos\theta$ and $r_e = b\sin\theta$ (see Fig. 10.16) so that

$$A\left(\mathbf{e}_i^{\beta};-\mathbf{e}_i^{\beta}\right) = \frac{ib\cos\theta}{2\sin\theta} J_1\left(2k_\beta b\sin\theta\right). \tag{10.36}$$

Figure 10.17 plots the behavior of the P-wave pulse-echo circular crack response (Eq. (10.36)) for a 1 mm radius crack in steel at an angle of incidence $\theta = 10^\circ$. Unlike a spherical void the crack response has very strong oscillations that decrease with increasing frequency. At normal incidence, however, the crack scattering response is quite different. In the pitch-catch case we can have a similar situation. We will call either of these special cases "generalized normal incidence". At generalized normal incidence $\mathbf{e}_q^{\alpha;\beta}$ is parallel to the crack normal, **n**. In the pulse-echo case this simply implies that the incident wave direction, $\mathbf{e}_i^{\beta}$, is parallel to **n** (Fig. 10.18). In either case we have $r_e \to 0$ and $\theta \to 0$ so that Eq. (10.34) for the pitch-catch case becomes

$$A\left(\mathbf{e}_i^{\beta};\mathbf{e}_s^{\alpha}\right) = \frac{ik_\alpha b^2 C^{\alpha;\beta}}{2} \tag{10.37}$$

and for the pulse-echo case

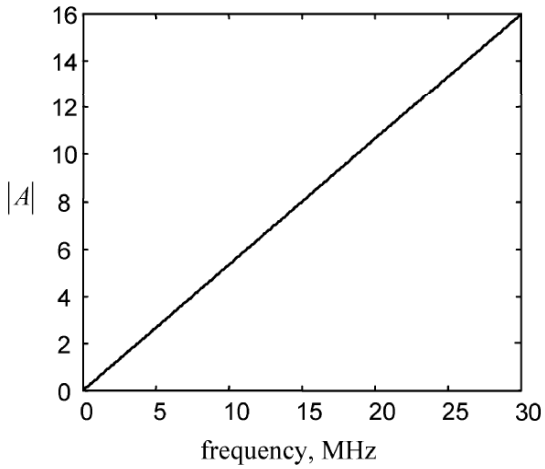

Fig. 10.19. The magnitude of the P-wave pulse-echo far-field scattering amplitude versus frequency calculated in the Kirchhoff approximation for a 1 mm radius circular crack in steel at normal incidence.

$$A\left(\mathbf{e}_i^{\beta};-\mathbf{e}_i^{\beta}\right)=\frac{ik_{\beta}b^2}{2} \tag{10.38}$$

so that the crack response increases linearly with frequency as shown in Figure 10.19.

We can understand some of this frequency domain behavior if we Fourier transform our results back into the time domain to obtain the crack impulse response. From Eq. (10.35) for the pulse-echo response of the elliptical crack, for example, we find for the case when the incident wave direction is at oblique incidence to the crack normal [Fundamentals]

$$a\left(\mathbf{e}_i^{\beta};-\mathbf{e}_i^{\beta},t\right)=\begin{cases}\dfrac{-b_1b_2c_{\beta}\left(\mathbf{e}_i^{\beta}\cdot\mathbf{n}\right)}{4\pi\left(r_e\right)^2}\dfrac{t}{\sqrt{\left(2r_e/c_{\beta}\right)^2-t^2}} & |t|\le 2r_e/c_{\beta}\\ 0 \quad otherwise\end{cases} \tag{10.39}$$

and for the normal incidence case, where

$$A\left(\mathbf{e}_i^{\beta};-\mathbf{e}_i^{\beta}\right)=\frac{ik_{\beta}b_1b_2}{2}, \tag{10.40}$$

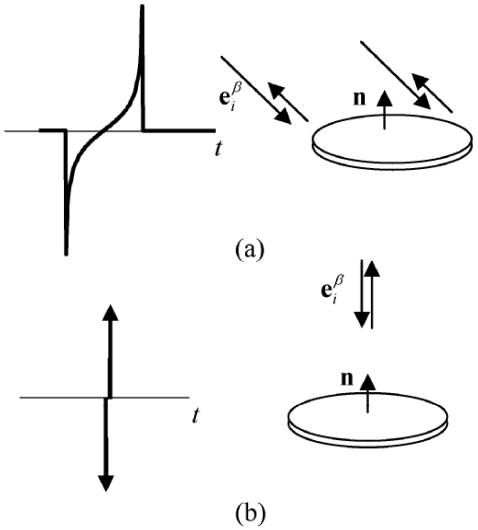

Fig. 10.20. (a) The time domain pulse-echo impulse response of an elliptical crack calculated in the Kirchhoff approximation at oblique incidence, and **(b)** at normal incidence.

we find

$$a\left(\mathbf{e}_i^\beta;-\mathbf{e}_i^\beta,t\right)=\frac{-b_1b_2}{2c_\beta}\frac{d\delta(t)}{dt}. \tag{10.41}$$

These cases are both plotted in Fig. 10.20. One can see that in the oblique incidence case (Fig. 10.20 (a)) the crack signal has an anti-symmetrical form, with two distinct peaks. These peaks are called crack *flashpoint* responses. The first flashpoint occurs when the incident wave front first touches the crack and the second flashpoint occurs when the incident wave front last touches the crack. The interference of the frequency components of these two flashpoint responses is what causes the strong oscillations in the frequency domain response for non-normal incidence. At normal incidence, the two flash point signals merge to form a "doublet" signal as shown in Fig. 10.20 (b). The doublet is represented by the derivative of a delta function, as given in Eq. (10.41). Note that since the Fourier transform of the delta function is just unity, we can write formally

$$\delta(t)=\frac{1}{2\pi}\int_{-\infty}^{+\infty}(1)\exp(-i\omega t)\,d\omega \tag{10.42}$$

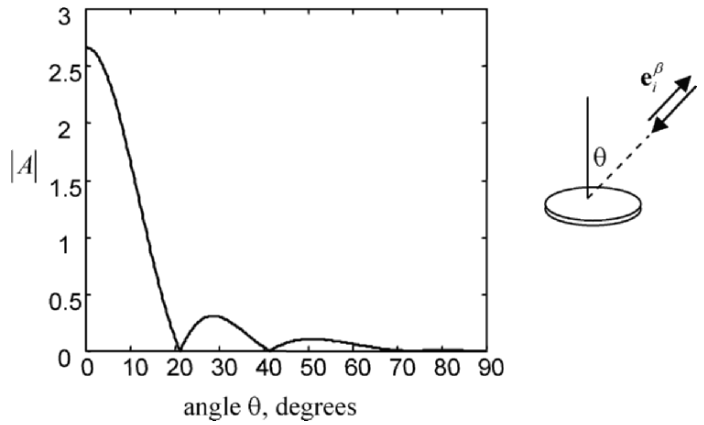

Fig. 10.21. The magnitude of the pulse-echo scattering amplitude response versus angle calculated in the Kirchhoff approximation for a 1 mm radius circular crack in steel at a frequency of 5 MHz.

from which we obtain

$$\frac{d\delta}{dt} = \frac{1}{2\pi}\int_{-\infty}^{+\infty}(-i\omega)\exp(-i\omega t)\,d\omega \tag{10.43}$$

Equation (10.43) shows that the Fourier transform of the derivative of the delta function is just $-i\omega$ so that taking the Fourier transform of Eq. (10.41), we do indeed obtain Eq. (10.40). Thus, the linearly increasing frequency domain response is just a consequence of having a doublet time domain response for the crack at normal incidence.

A flat crack is a very specular scatterer since in pulse-echo its scattering response is large when the incident wave strikes a crack at normal incidence but decreases rapidly as a function of the angle, θ, that the incident wave makes with the crack normal, as shown in Fig. 10.21.

10.5 Validity of the Kirchhoff Approximation

The Kirchhoff approximation is a very useful tool for modeling the scattering of volumetric flaws and cracks. For the volumetric flaw case, the Kirchhoff approximation predicts a leading edge response that is in fact

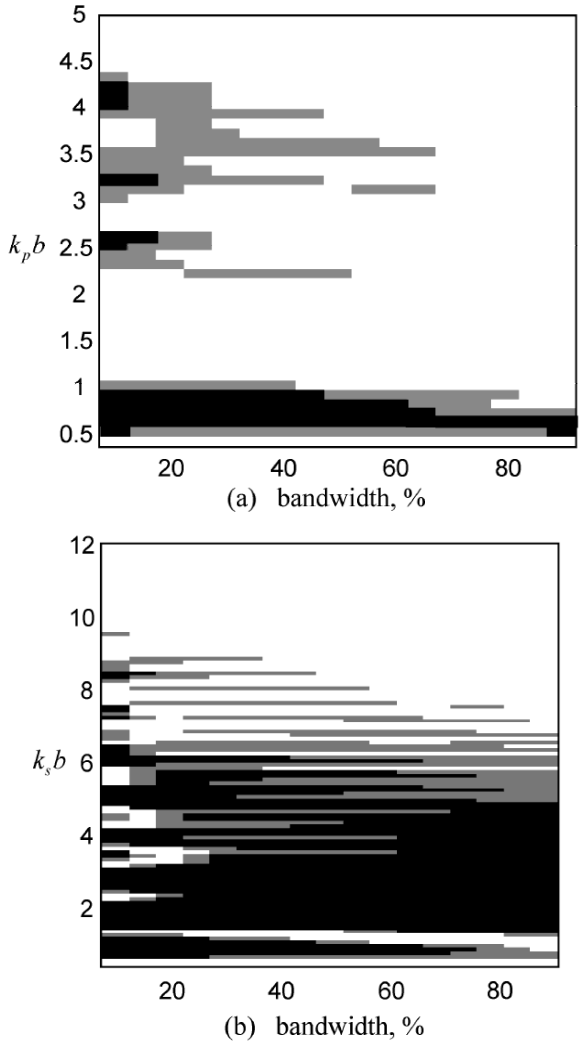

Fig. 10.22. A comparison of the peak-to-peak pulse-echo responses of a spherical void of radius b as calculated by the Kirchhoff approximation and the method of separation of variables where the non-dimensional wave number and bandwidth are varied. **(a)** Pulse-echo P-wave responses. **(b)** Pulse-echo SV-wave responses. White region: peak-to-peak differences < 1 dB, Gray region: differences > 1 dB and <1.5 dB, Black region: differences > 1.5 dB.

exact at high frequencies. Thus, as long as the flaw is not too small so that the later arriving waves can merge with this leading edge response or for special cases where the later arriving signals may be larger than the leading edge response, the Kirchhoff approximation will accurately model the amplitude of the flaw response, as measured, for example, by the maximum peak-to-peak amplitude of the time domain wave form. This fact can be demonstrated for the pulse-echo response of a spherical void by comparing wave forms synthesized by the method of separation of variables (discussed in section 10.8) and the Kirchhoff approximation. In this case the scattering amplitude was multiplied by a Gaussian window having a center frequency, f_c , and bandwidth, *bw*, (see Appendix A for an example). The result was then inverted into the time domain with a Fast Fourier Transform and the peak-to-peak value of the wave form was obtained. In order to compare the peak-to-peak values obtained in this fashion using either the method of separation of variables or the Kirchhoff approximation, it is necessary to have a practical criterion on when the Kirchhoff approximation is accurate. Since NDE inspection setups often have an uncertainty of 1-1.5 dB or greater in the amplitudes of the signals measured (due to experimental setup errors, noise, etc.) we will label the Kirchhoff approximate accurate if the peak-to-peak amplitude of the signal that it predicts is less than 1 dB different from the separation of variables result.

Figures 10.22 (a), (b) shows the results of simulating the peak-to-peak pulse-echo P-wave and SV-wave responses of a spherical void of radius *b* at different Gaussian window center frequencies and bandwidths. The white region in that figure is where the Kirchhoff and separation of variables solutions agree within 1 dB while the gray region is where the responses differ by more than 1 dB but less than 1.5 dB, and the black region is where the responses differ by 1.5 dB or more. The non-dimensional wave numbers, $k_p b = 2\pi f_c b / c_p$ and $k_s b = 2\pi f_c b / c_s$ shown in Fig. 10.22 were computed at the center frequency, f_c , of the Gaussian window and the bandwidth is given as a percentage of that center frequency value. For the P-wave case for values of $k_p b > 4.5$ it was found that the Kirchhoff approximation was accurate for all bandwidths but that below this value the bandwidth began to also play a role. However, for sufficiently large bandwidths Fig. 10.22 (a) shows that the Kirchhoff approximation remains accurate to wave numbers as small as $k_p b = 1$ in the P-wave case. At wave numbers $k_p b < 1$ there may be cases where the differences also are less than 1 dB but these only arise accidentally from

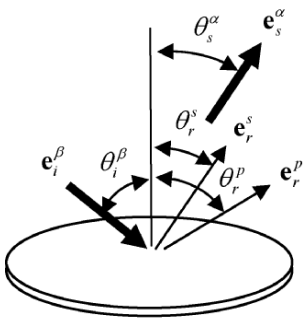

Fig. 10.23. In a general pitch-catch setup a flat crack generates a large specularly scattered signal when the scattered wave direction (and wave type) coincides with one of the reflected wave directions (and wave type) as determined by Snell's law, i.e. where $\theta_s^s = \theta_r^s$ or $\theta_s^p = \theta_r^p$ and where the reflected angles, θ_r^p, θ_r^s are given in terms of the incident angle, θ_i^β, by the relations $\sin\theta_r^p = \left(c_p / c_\beta\right)\sin\theta_i^\beta$, $\sin\theta_r^s = \left(c_s / c_\beta\right)\sin\theta_i^\beta$.

canceling errors since the Kirchhoff approximation and exact solution can be shown analytically to have different low frequency limits. Figure 10.22 (b) shows that in the case of shear waves, the wave number $k_s b$ must be greater than 10 for the Kirchhoff approximation to remain valid for all bandwidths and that from $k_s b = 10$ to $k_s b = 6$ approximately there are bandwidths effects.

Thus, while formally the Kirchhoff is a high frequency approximation where one assumes $kb >> 1$, we see that this approximation remains useful and accurate in predicting pulse-echo peak-to-peak signal amplitudes for spherical voids at much lower frequencies and/or flaw sizes. It is also clear from Fig. 10.22 that bandwidth as well as frequency/size plays a role in how well the Kirchhoff approximation can perform.

For ideal flat cracks, the Kirchhoff approximation also accurately models the pulse-echo amplitude of the crack response when the incident wave direction is normal to the crack or in pitch-catch when the scattered wave direction is along a reflected wave direction as predicted by Snell's law (see Fig. 10.23). In either of these generalized normal incidence cases, as discussed previously, the vector $\mathbf{g}^{\alpha;\beta} = \left(c_\alpha / c_\beta\right)\mathbf{e}_i^\beta - \mathbf{e}_s^\alpha$ is parallel to the crack normal **n**. The expression for the scattering of a flat crack, Eq. (10.28), can be written in terms of this vector as:

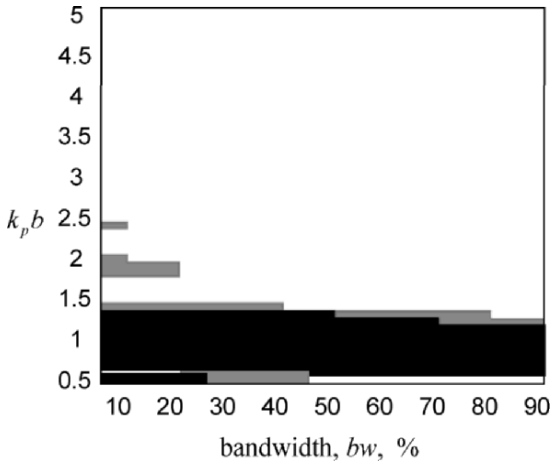

Fig. 10.24. A comparison of the normal incidence peak-to-peak pulse-echo P-wave responses of a circular crack of radius b as calculated by the Kirchhoff approximation and the method of separation of variables where the non-dimensional wave number, $k_p b$, and bandwidth, bw, are varied. White region: peak-to-peak differences < 1 dB, Light gray region: differences > 1 dB and <1.5 dB, Black region: differences > 1.5 dB.

$$A\left(\mathbf{e}_i^{\beta};\mathbf{e}_s^{\alpha}\right)=\frac{ik_{\alpha}C^{\alpha;\beta}}{2\pi}\int_S \exp\left[ik_{\alpha}\mathbf{g}^{\alpha;\beta}\cdot\mathbf{x}_s\right]dS\left(\mathbf{x}_s\right). \tag{10.44}$$

But $\mathbf{x}_s$ is a point lying in the plane of the crack and so we have $\mathbf{g}^{\alpha;\beta}\cdot\mathbf{x}_s=0$ and Eq. (10.44) becomes for an arbitrarily shaped flat crack (see Eqs. (10.37), (10.38), (10.40) for the same result for different special shapes or setups)

$$A\left(\mathbf{e}_i^{\beta};\mathbf{e}_s^{\alpha}\right)=\frac{ik_{\alpha}C^{\alpha;\beta}S_f}{2\pi}, \tag{10.45}$$

where S_f is the area of the flat crack. For all the cases where Eq. (10.45) holds we see a large specular response (like the doublet response shown earlier) that agrees with more exact scattering model predictions. Note that for a shear wave incident on the crack beyond the critical angle where the reflected P-wave disappears, the scattered S-wave response predicted by Eq. (10.45) will include pulse distortion since the coefficient $C^{\alpha;\beta}$ is then

complex [Fundamentals]. Such pulse distortion, however, may be difficult to see in practice since at these angles the amplitude of the crack response will be small.

We can also examine the accuracy of the Kirchhoff approximation in predicting the pulse-echo normal incidence response of a circular crack in the same fashion as done for a spherical void. In this case, there is no separation of variables solution to compare to, but there have been numerical calculations done with the method of optimal truncation (MOOT) [10.34] for the pulse-echo P-wave response of a circular crack that can be used as an "exact" reference solution. Figure 10.24 shows the results of generating pulse-echo normal incidence P-wave peak-to-peak responses of a circular crack of radius b at different wave numbers, $k_p b = 2\pi f_c b / c_p$, and bandwidths, bw using the Kirchhoff approximation and MOOT. It can be seen from that figure that for wave numbers $k_p b > 2.5$ the Kirchhoff approximation is accurate for all bandwidths but bandwidth begins to play a role for smaller wave numbers. However, for sufficiently large bandwidths the Kirchhoff approximation remains accurate to non-dimensional wave numbers as small as $k_p b = 1.5$. At smaller wave numbers the Kirchhoff approximation is generally inaccurate although again there may be cases where canceling errors occur. These results demonstrate that, as in the spherical void case, the Kirchhoff approximation remains accurate for cases where the condition $kb >> 1$ is not satisfied and that bandwidth also plays a role in determining when the Kirchhoff approximation is accurate but it is not as strong a factor as in the spherical void case.

For pulse-echo cases where the incident waves are not normal to the crack the Kirchhoff approximation predicts time domain flash point responses from the crack tips (see Fig. 10.20 (a)). It is commonly stated that the amplitudes of these signals do not agree with more exact scattering calculations except in a relatively small angular range (of about 20-30 degrees) from normal incidence [10.2]. However, this conclusion has been reached by considering either single frequency results or simulating narrow bandwidth time domain responses. It will be shown here that bandwidth plays an important role in determining the angular range over which the Kirchhoff approximation can accurately predict the pulse-echo peak-to-peak response of a circular crack. This fact is demonstrated by simulating oblique incident pulse-echo scattered P-wave responses of a circular crack with both the Kirchhoff approximation and MOOT and then comparing their predicted time domain peak-to-peak crack responses. In this study a Gaussian window having a center frequency of 10 MHz was

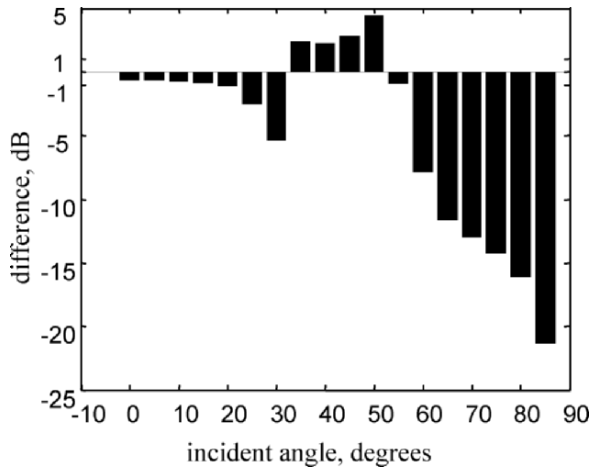

Fig. 10.25. Differences in dB between predicted peak-to-peak pulse-echo P-wave responses of a 0.381 mm radius circular crack in steel as calculated by the Kirchhoff approximation and by MOOT for a narrow band (2 MHz bandwidth, 10 MHz center frequency) system response.

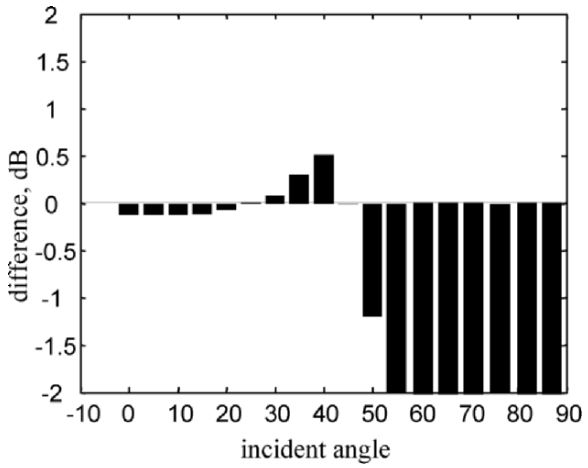

Fig. 10.26. Differences in dB between predicted peak-to-peak pulse-echo P-wave responses of a 0.381 mm radius circular crack in steel as calculated by the Kirchhoff approximation and by MOOT for a relatively wide band (6 MHz bandwidth, 10 MHz center frequency) system response. [For angles greater than 50° the differences are larger in magnitude than 2 dB so their values are off the scale of this figure.]

used with a flaw size of $b = 0.381$ mm. The compressional wave speed was taken as 6200 m/sec so that in all the cases considered the non-dimensional wave number was fixed at $k_p b = 3.86$. This wave number value is sufficiently large so that at normal incidence there were no bandwidth effects (see Fig. 10.24) but for oblique incidence this is not the case. For example, Fig. 10.25 shows the differences in dB between predicted peak-to-peak pulse-echo P-wave responses of the crack as calculated with the Kirchhoff approximation and MOOT and plotted versus angle of incidence for a narrow bandwidth (20%) window. In this case, differences exceeded 1 dB at an angle of incidence of about 20 degrees. However, if the bandwidth of the window is changed to 60%, holding all other variables fixed, the differences remain smaller than 1 dB for angles as large as 45 degrees, as shown in Fig. 10.26. For larger bandwidths, the range of angles where the Kirchhoff approximation is accurate is even larger. We have found that the precise way in which the angular range of accuracy of the Kirchhoff approximation varies is highly dependent on both the wave number and bandwidth so it is difficult to display comprehensible results for a wide range of cases on a single graph. Figure 10.27 shows a plot of the maximum incident angle at which the Kirchhoff approximation is accurate (i.e. within 1 dB of the MOOT solution) versus bandwidth for a

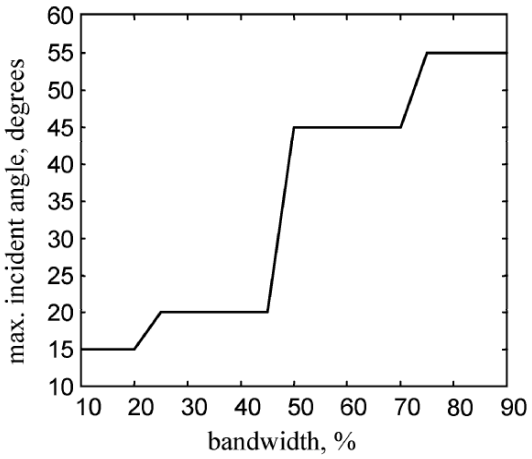

Fig. 10.27. The maximum incident angle at which the peak-to-peak pulse-echo flaw response predicted by the Kirchhoff approximation remains within 1 dB of the MOOT solution as a function of the bandwidth for the case of a P-wave obliquely incident on a 0.381 mm radius crack in steel ($k_p b$ = 5.0).

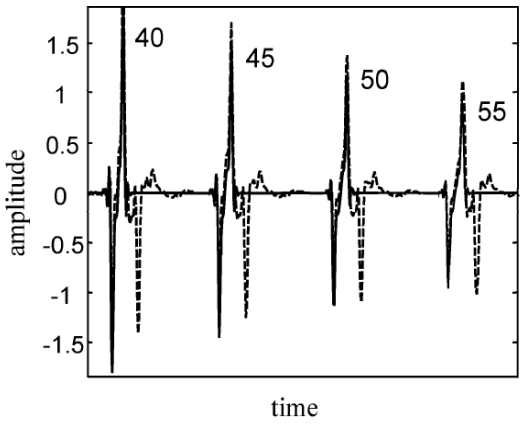

Fig. 10.28. Very wide-band simulated P-wave pulse-echo responses for a 0.381 mm radius crack in steel for angles of 40, 45, 50, and 55 degrees. Kirchhoff approximation (solid line), MOOT solution (dashed line).

non-dimensional wave number $k_p b = 5.0$. Although the curves at other wave numbers have different shapes, the trend shown in Fig. 10.27 remains the same for those other cases, namely the angular range where the Kirchhoff approximation is accurate can be as small as 15-20 degrees for very narrow bandwidth systems but as high as 55-60 degrees for very wide band systems.

To understand why the Kirchhoff approximation works better as the bandwidth increases consider Fig. 10.28 which shows a series of wave forms simulated by the Kirchhoff approximation and MOOT for the same 0.381 mm radius crack case examined in Fig. 10.27 but where all frequencies from 0-20 MHz were retained in calculating the time domain responses, yielding a very high bandwidth response. From Fig. 10.28 it can be seen that for angles from 40 to 55 degrees the flash point responses predicted by the Kirchhoff approximation agree well with those of the MOOT solution although the Kirchhoff approximation does predict a somewhat smaller trailing flashpoint signal than MOOT. Up to the 55 degree angle case the flashpoint signals are the largest signals present in the crack response but the MOOT solution also contains later arriving responses not predicted by the Kirchhoff approximation that grow as the angle increases. As the bandwidth decreases, these later arriving waves merge with the flashpoint responses, generating peak-to-peak responses that can differ significantly from the Kirchhoff approximation, which only contains the flashpoint signals.

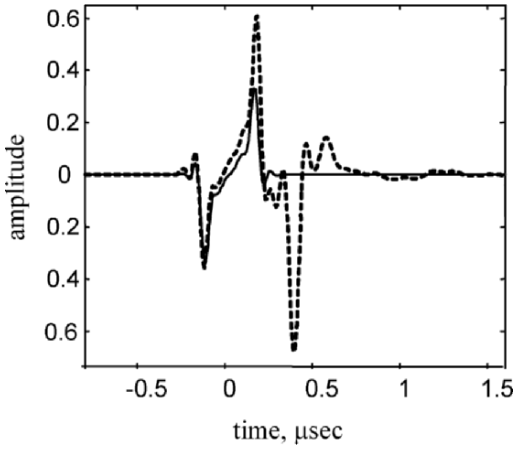

Fig. 10.29. A very wide-band simulated P-wave pulse-echo responses for a 0.381 mm radius crack in steel for an incident angle of 75 degrees. Kirchhoff approximation (solid line), MOOT solution (dashed line).

Ultimately the Kirchhoff approximation must fail at very high angles since in this approximation the flash point signals go to zero as the incident angle approaches 90 degrees while the exact solution remains finite. As an example of a very high angle case consider the flaw response at an angle of 75 degrees as shown in Fig. 10.29. At this angle the trailing flashpoint response predicted by the Kirchhoff approximation is much smaller than that given by the MOOT solution and the later arriving waves now are larger than either of the flashpoint responses so that the peak-to-peak response predicted by the Kirchhoff approximation is significantly in error. But as can be seen in Fig. 10.29 the Kirchhoff approximation continues to accurately model the first arriving flashpoint signal. It can also be seen from Fig. 10.29 that even for this angle the Kirchhoff approximation continues to model the arrival times of both flash point signals accurately. The arrival times of such crack tip signals are used in crack sizing methods such as the time-of-flight- diffraction (TOFD) method [10.3] and equivalent flaw sizing methods [Fundamentals], so the Kirchhoff approximation can be reliably used as the basis for those sizing methods.

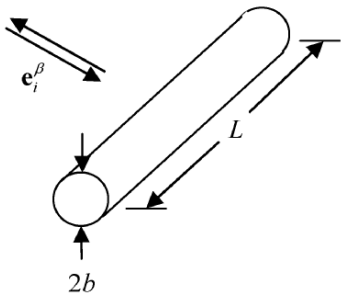

Fig. 10.30. The pulse-echo scattering of a cylindrical side-drilled hole of radius b and length L. The incident wave direction, $\mathbf{e}_i^\beta$, is assumed to lie in a plane perpendicular to the axis of the cylinder.

10.6 The Kirchhoff Approximation for Side-drilled Holes

Another scattering geometry that is commonly used in NDE calibration experiments is the side-drilled hole. This is a case where we can also obtain explicit results for the scattering amplitude in the Kirchhoff approximation. We will give the derivation here since it is not readily available in the literature. Consider the case of pulse-echo where the axis of a side-drilled hole of radius b and length L is normal to the plane of incidence (the plane containing the incident wave direction and the normal to the curved side of the side-drilled hole (Fig. 10.30). Equation (10.12) is again applicable to this case so the response of the side-drilled hole in the Kirchhoff approximation is given by

$$A\left(\mathbf{e}_i^\beta;-\mathbf{e}_i^\beta\right)=\frac{-ik_\beta}{2\pi}\int_{S_{lit}}\left(\mathbf{e}_i^\beta\cdot\mathbf{n}\right)\exp\left(2ik_\beta\mathbf{x}_s\cdot\mathbf{e}_i^\beta\right)dS\left(\mathbf{x}_s\right). \tag{10.46}$$

Now, consider a surface S' that extends the lit surface to infinity in the $\mathbf{e}_i^\beta$ direction and a surface at infinity, S^∞, that closes this extended surface as shown in Fig. 10.31. Since $\mathbf{e}_i^\beta\cdot\mathbf{n}=0$ on S' and the integrand on S^∞ will

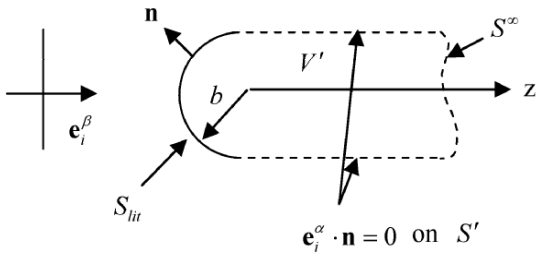

Fig. 10.31. The cross-section of the side-drilled hole showing the lit surface, S_{lit}, and the extension of that surface by the surfaces S' and S^∞ to enclose the volume V'.

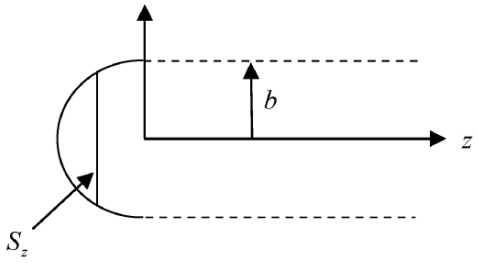

Fig. 10.32. The cross-sectional area, S_z, for the side-drilled hole geometry.

vanish if we add a small amount of damping to the plane wave term $\exp\left(2ik_\beta \mathbf{x}_s \cdot \mathbf{e}_i^\beta\right)$, we can write

$$A\left(\mathbf{e}_i^\beta; -\mathbf{e}_i^\beta\right) = \frac{-ik_\beta}{2\pi} \int\limits_{S_{lit}+S'+S^\infty} \left(\mathbf{e}_i^\beta \cdot \mathbf{n}\right) \exp\left(2ik_\beta \mathbf{x}_s \cdot \mathbf{e}_i^\beta\right) dS\left(\mathbf{x}_s\right) \tag{10.47}$$

and then use the divergence theorem to write the integral over the closed surface in Eq. (10.47) as a volume integral over the volume V' within this closed surface:

$$A\left(\mathbf{e}_i^\beta; -\mathbf{e}_i^\beta\right) = \frac{k_\beta^2}{\pi} \int\limits_{V'} \exp\left(2ik_\beta \mathbf{e}_i^\beta \cdot \mathbf{x}\right) dV. \tag{10.48}$$

If we take the z-axis as along the incident wave direction then $\mathbf{e}_i^\beta \cdot \mathbf{x} = z$ and we can write the volume element as $dV = S_z(z)\,dz$ where $S_z(z)$ is the cross-sectional area of the volume perpendicular to $\mathbf{e}_i^\beta$. For the volume V', however, we have directly from the geometry (see Fig. 10.32)

$$S_z(z) = \begin{cases} 0 & z < -b \\ 2L\sqrt{b^2 - z^2} & -b < z < 0 \\ 2Lb & z > 0 \end{cases} \tag{10.49}$$

so that Eq. (10.48) becomes

$$\begin{aligned} A\left(\mathbf{e}_i^\beta; -\mathbf{e}_i^\beta\right) = {} & \frac{2Lk_\beta^2}{\pi}\int_{-b}^{0}\sqrt{b^2 - z^2}\,\exp\left(2ik_\beta z\right)dz \\ & + \frac{2Lbk_\beta^2}{\pi}\int_0^\infty \exp\left(2ik_\beta z\right)dz. \end{aligned} \tag{10.50}$$

In the first integral in Eq. (10.50) let $x = -z/b$ and perform the integration explicitly for the second integral, again ignoring the limit at infinity by adding a small amount of damping to the complex exponential. We find

$$A\left(\mathbf{e}_i^\beta; -\mathbf{e}_i^\beta\right) = \frac{2L\left(k_\beta b\right)^2}{\pi}\int_0^1\sqrt{1 - x^2}\,\exp\left(-2ik_\beta bx\right)dx + \frac{iLbk_\beta}{\pi}. \tag{10.51}$$

But from Gradshteyn and Ryzhik [10.4]

$$\begin{aligned} \int_0^1\sqrt{1 - x^2}\,\cos\left(2kbx\right)dx &= \frac{\sqrt{\pi}}{2}\left(\frac{1}{kb}\right)\Gamma\left(\frac{3}{2}\right)J_1\left(2kb\right) \\ \int_0^1\sqrt{1 - x^2}\,\sin\left(2kbx\right)dx &= \frac{\sqrt{\pi}}{2}\left(\frac{1}{kb}\right)\Gamma\left(\frac{3}{2}\right)S_1\left(2kb\right) \end{aligned} \tag{10.52}$$

and $\Gamma\left(\frac{3}{2}\right) = \frac{\sqrt{\pi}}{2}$ so that

$$A\left(\mathbf{e}_i^\beta; -\mathbf{e}_i^\beta\right) = \frac{\left(k_\beta b\right)L}{2}\left[J_1\left(2k_\beta b\right) - iS_1\left(2k_\beta b\right)\right] + \frac{i\left(k_\beta b\right)L}{\pi}, \tag{10.53}$$

where J_1 is a Bessel function of order one and S_1 is a Struve function of order one. Since these special functions can be easily calculated numerically,

Eq. (10.53) gives us an explicit expression for the pulse-echo scattering amplitude of the side-drilled hole. At high frequencies [10.5]

$$\begin{aligned} S_1(2kb) &\cong Y_1(2kb) + \frac{2}{\pi} + O\left(\frac{1}{kb}\right)^2 \\ J_1(2kb) - iY_1(2kb) &= H_1^{(2)}(2kb) \\ &\cong \sqrt{\frac{1}{\pi kb}} \exp\left[i(3\pi/4 - 2kb)\right], \end{aligned} \tag{10.54}$$

where $H_1^{(2)}$ is a Hankel function of the second kind of order one and Y_1 is a Bessel function of the second kind of order one. Placing these approximations into Eq. (10.53), at high frequencies the pulse-echo scattering amplitude is given by

$$A\left(\mathbf{e}_i^\beta; -\mathbf{e}_i^\beta\right) \cong \frac{L}{2}\sqrt{\frac{k_\beta b}{\pi}} \exp\left[i(3\pi/4 - 2k_\beta b)\right]. \tag{10.55}$$

At low frequencies, we have instead

$$\begin{aligned} J_1(2kb) &\cong \frac{kb}{\Gamma(2)} = kb \\ S_1(2kb) &\cong \frac{8}{3\pi}(kb)^2 \end{aligned} \tag{10.56}$$

so that the scattering amplitude becomes

$$A\left(\mathbf{e}_i^\beta; -\mathbf{e}_i^\beta\right) \cong \frac{ik_\beta bL}{\pi} \tag{10.57}$$

although we cannot expect the Kirchhoff approximation to be valid at these low frequencies.

Figures 10.33, 10.34 plot the magnitude and phase of the normalized pulse echo scattering amplitude versus wave number from the Kirchhoff solution, Eq. (10.53), and compares these results to the exact separation of variables solution for the two-dimensional pulse-echo P-wave scattering amplitude [10.6]. It can be seen that the Kirchhoff approximation agrees well with the separation of variables solution, particularly at the higher frequencies. In Fig. 10.33 both solutions approximately follow the high frequency square root behavior in frequency given by Eq. (10.55). The exact separation of variables solution has more oscillations than the Kirchhoff approximation since, like the spherical void case, the exact solution oscillations here come from the interference of the

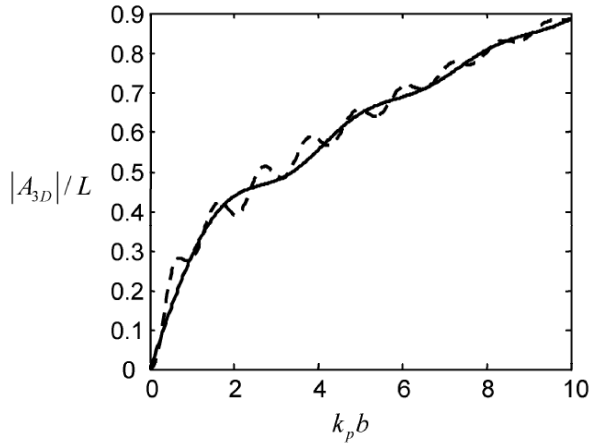

Fig. 10.33. The three-dimensional normalized pulse-echo P-wave scattering amplitude versus normalized wave number for a side drilled hole in the Kirchhoff approximation (solid line) and from the exact separation of variables solution (dashed line).

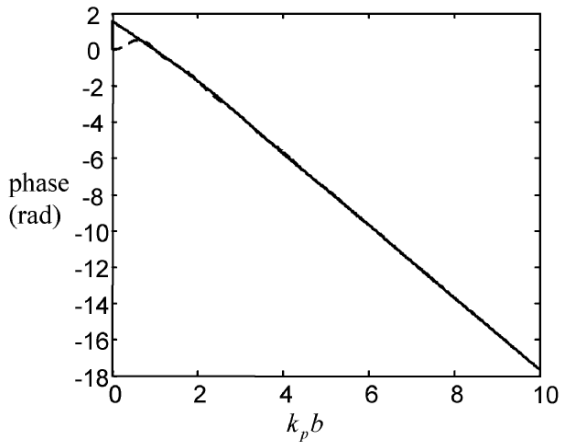

Fig. 10.34. The phase of the three-dimensional normalized pulse-echo P-wave scattering amplitude versus normalized wave number for a side drilled hole in the Kirchhoff approximation (solid line) and from the exact separation of variables solution (dashed line).

leading edge response of the side-drilled hole with a creeping wave that is not contained in the Kirchhoff approximation.

Since our Kirchhoff solution was obtained by considering the response of a three-dimensional cylinder of length L while the separation of variables solution is for the two-dimensional scattering from an infinitely long cylinder, some remarks are needed to describe how we made the comparison shown in Figs. 10.33 and 10.34. In two-dimensional scattering problems the waves in the far-field of the scatterer are not spherical waves but cylindrical waves and the two dimensional far-field scattering displacement $\mathbf{u}^{scatt} = \left(u_1^{scatt}, u_2^{scatt}\right)$ is given by [Fundamentals]

$$\mathbf{u}^{scatt}\left(\mathbf{y},\omega\right) = U_0 \frac{\tilde{\mathbf{A}}\left(\mathbf{e}_i^{\beta};\mathbf{e}_s^{p}\right)}{\sqrt{R_s}} \exp\left(ik_p R_s\right) + U_0 \frac{\tilde{\mathbf{A}}\left(\mathbf{e}_i^{\beta};\mathbf{e}_s^{s}\right)}{\sqrt{R_s}} \exp\left(ik_s R_s\right), \quad (10.58)$$

where the scattering amplitudes, $\tilde{\mathbf{A}}\left(\mathbf{e}_i^{\beta};\mathbf{e}_s^{\alpha}\right)$, now are two-dimensional vectors and all the distances also are measured in a two dimensional space $\left(y_1, y_2\right)$. In this case, if we compute the same component of the scattering amplitude as done for the three-dimensional case, we obtain

$$A_{2D}\left(\mathbf{e}_i^{\beta};\mathbf{e}_s^{\alpha}\right) = \tilde{\mathbf{A}}\left(\mathbf{e}_i^{\beta};\mathbf{e}_s^{\alpha}\right)\cdot\left(-\mathbf{d}^{\alpha}\right), \quad (10.59)$$

where we use the "2D" label to emphasize that the calculation is for the two-dimensional scattering amplitude. It can be shown that this component is given by [Fundamentals]

$$A_{2D}\left(\mathbf{e}_i^{\beta};\mathbf{e}_s^{\alpha}\right) = \sqrt{\frac{i}{8\pi k_\alpha}} \frac{1}{\rho c_\alpha^2} \int_C d_\sigma^\alpha \left[\tilde{\tau}_{\gamma\sigma} n_\gamma + ik_\alpha C_{\sigma\delta\gamma\nu} e_{s\delta}^{\alpha} n_\gamma \tilde{u}_\nu\right] \cdot \exp\left[-ik_\alpha e_{s\lambda}^{\alpha} y_\lambda\right] dc, \quad (10.60)$$

(no sum on s, α)

where n_γ are the components of the outward normal to the flaw and the integration is a counterclockwise line integral around the edge of the two-dimensional scatterer. All the repeated Greek subscripts in Eq. (10.60) are summed over the values (1,2) only (no sum on s, α). Recall Eq. (10.7) for the same three-dimensional scattering amplitude component is given by

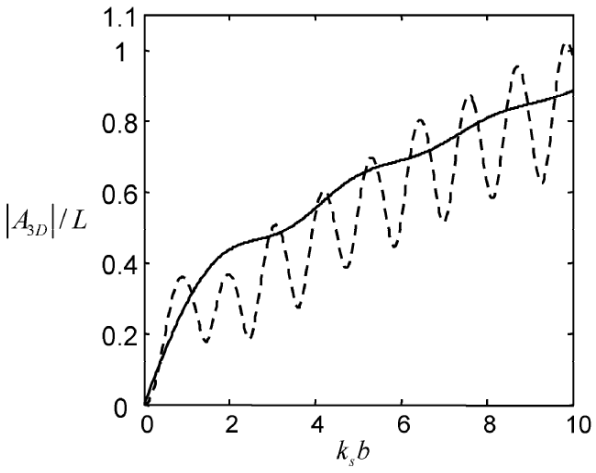

Fig. 10.35. The three-dimensional normalized pulse-echo SV-wave scattering amplitude versus normalized wave number for a side drilled hole in the Kirchhoff approximation (solid line) and from the exact separation of variables solution (dashed line).

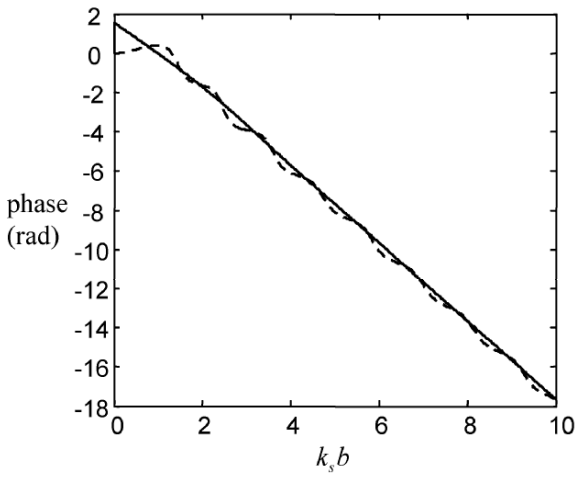

Fig. 10.36. The phase of the three-dimensional normalized pulse-echo SV-wave scattering amplitude versus normalized wave number for a side drilled hole in the Kirchhoff approximation (solid line) and from the exact separation of variables solution (dashed line).

$$A_{3D}\left(\mathbf{e}_i^{\beta};\mathbf{e}_s^{\alpha}\right)=\frac{1}{4\pi\rho c_{\alpha}^2}\int_S d_l^{\alpha}\left[\tilde{\tau}_{lk}n_k+ik_{\alpha}C_{lkpj}e_{sk}^{\alpha}n_p\tilde{u}_j\right]\cdot\exp\left(-ik_{\alpha}\mathbf{x}_s\cdot\mathbf{e}_s^{\alpha}\right)dS\left(\mathbf{x}_s\right). \tag{10.61}$$

(no sum on s, α)

From Eqs. (10.60) and (10.61) we see that the two- and three-dimensional forms are very similar. In fact, if in the three-dimensional case the geometry and fields were all two-dimensional, i.e. if we set $n_3=d_3^{\alpha}=e_{s3}^{\alpha}=\tilde{u}_3=0$ and assume $\tilde{\tau}_{\alpha\beta}=\tilde{\tau}_{\alpha\beta}\left(y_1,y_2,\omega\right)$, $\tilde{u}_{\beta}=\tilde{u}_{\beta}\left(y_1,y_2,\omega\right)$ we would obtain

$$A_{3D}\left(\mathbf{e}_i^{\beta};\mathbf{e}_s^{\alpha}\right)=\frac{L}{4\pi\rho c_{\alpha}^2}\int_S d_{\sigma}^{\alpha}\left[\tilde{\tau}_{\gamma\sigma}n_{\gamma}+ik_{\alpha}C_{\sigma\delta\gamma\nu}e_{s\delta}^{\alpha}n_{\gamma}\tilde{u}_{\nu}\right]\cdot\exp\left(-ik_{\alpha}e_{s\lambda}^{\alpha}y_{\lambda}\right)dc. \tag{10.62}$$

(no sum on s, α)

Note that all these assumptions are fulfilled exactly by our three-dimensional solution for the side-drilled hole in the Kirchhoff approximation. These are also reasonable assumptions for more general scattering calculations if we assume the incident wave is a quasi-plane wave propagating in a plane which is perpendicular to the axis of the side-drilled hole. Comparing Eqs. (10.60) and (10.62) we find

$$A_{2D}\left(\mathbf{e}_i^{\beta};\mathbf{e}_s^{\alpha}\right)=\left(\frac{2\mathrm{i}\pi}{k_{\alpha}}\right)^{1/2}\frac{A_{3D}\left(\mathbf{e}_i^{\beta};\mathbf{e}_s^{\alpha}\right)}{L}. \tag{10.63}$$

Equation (10.63) was used to transform the two-dimensional separation of variables scattering amplitude, A_{2D}, into an equivalent three-dimensional scattering amplitude, A_{3D}. In Figs. 10.33 and 10.34 the magnitude and phase of this exact three-dimensional amplitude was plotted and compared with the Kirchhoff solution. Thus, the quantities being plotted for both curves in those figures are based on A_{3D}/L. Figures 10.35 and 10.36 show the corresponding results for the pulse-echo scattering amplitude of the side-drilled hole calculated for shear (SV) waves. In this case the exact solution has deep oscillations since stronger SV- creep waves are generated than in the P-wave case. The Kirchhoff solution is unchanged in

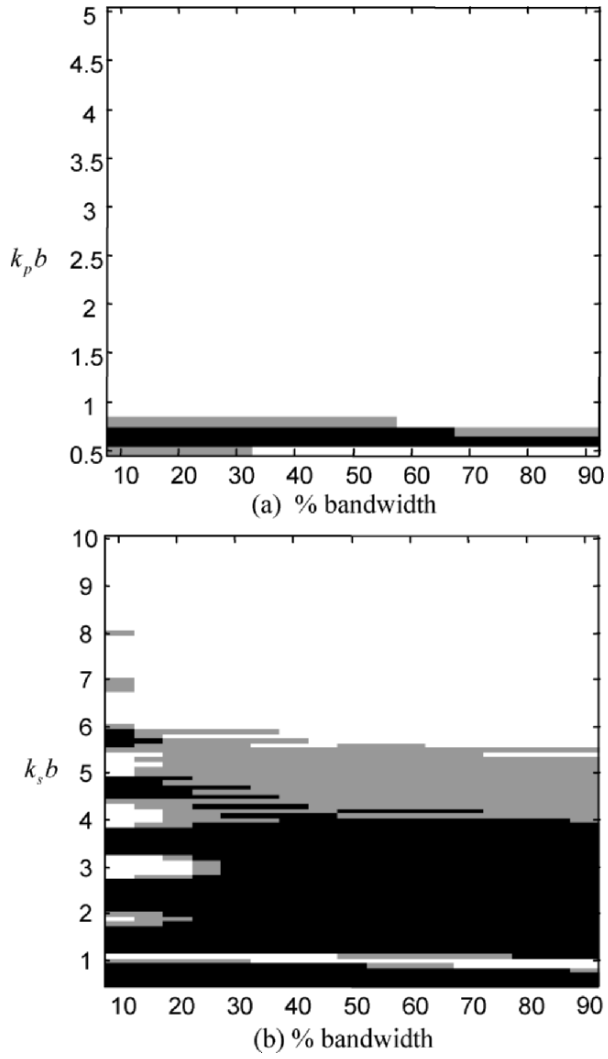

Fig. 10.37. A comparison of the peak-to-peak pulse-echo responses of a side drilled hole of radius b as calculated by the Kirchhoff approximation and the method of separation of variables where the non-dimensional wave number and bandwidth are varied. **(a)** Pulse-echo P-wave responses, **(b)** pulse-echo SV-wave responses. White region: peak-to-peak differences < 1 dB, Gray region: differences > 1 dB and <1.5 dB, Black region: differences > 1.5 dB.

form since Eq. (10.53) is applicable to both P- and SV-waves, but the normalized wave number appearing in the SV-wave case is $k_s b$.

The accuracy of the Kirchhoff approximation for the side drilled hole can also be studied as a function of the wave number and bandwidth as done with the spherical void. Like the spherical void, there is an exact separation of variables solution available for a cylindrical void that can be used to test the accuracy of the Kirchhoff approximation (see section 10.8). Figures 10.37 (a), (b) show the regions of validity of the Kirchhoff approximation for the side drilled hole that were obtained in the same fashion as Figs. 10.23 and 10.24 for the spheroid void and crack, respectively. Figure 10.37 (a) shows that for the pulse-echo P-wave case, the Kirchhoff approximation for the peak-to-peak response of the side drilled hole remains accurate (within 1 dB of the exact solution) for wave numbers even smaller than one and that there are virtually no bandwidth effects. In contrast the pulse-echo SV-wave response begins to show some small bandwidth effects at $k_s b =$ 8 and the Kirchhoff approximation becomes inaccurate at all bandwidths for $k_s b < 4$, approximately.

10.7 The Born Approximation

Another approximation that is useful for simulating flaw scattering responses is the Born approximation [Fundamentals], [10.7-10.11]. This approximation is formally a low frequency, weak scattering approximation but we will show that with some modifications it may be applicable under a wider set of conditions. The Born approximation uses an exact volume integral representation of the far-field scattering amplitude given by [Fundamentals]

$$A\left(\mathbf{e}_i^{\beta};\mathbf{e}_s^{\alpha}\right)=\frac{-d_q^{\alpha}}{4\pi\rho c_{\alpha}^2}\int_{V_f}\left[\Delta\rho\,\omega^2\tilde{u}_q+ik_{\alpha}e_{sk}^{\alpha}\Delta C_{kqmj}\frac{\partial\tilde{u}_m}{\partial x_j}\right]\cdot\exp\left(-ik_{\alpha}\mathbf{x}\cdot\mathbf{e}_s^{\alpha}\right)dV\left(\mathbf{x}\right) \qquad (10.64)$$

(no sum on s, α)

where V_f is the volume of the flaw. In Eq. (10.64) $\Delta\rho=\rho_f\left(\mathbf{x}\right)-\rho$, $\Delta C_{kqmj}=C_{kqmj}^f\left(\mathbf{x}\right)-C_{kqmj}$, where $\rho_f\left(\mathbf{x}\right), C_{kqmj}^f\left(\mathbf{x}\right)$ are the density and elastic constants of the flaw (both of which can vary with position in the

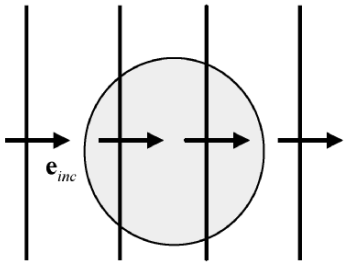

Fig. 10.38. The Born approximation assumes that for a weakly scattering inclusion, the fields in the flaw are to first order the fields of the incident wave traveling in the host material as if the flaw was not present, as shown.

flaw) while ρ and C_{kqmj} are the density and elastic constants of the host material surrounding the flaw (both of which are assumed to be constants, i.e. the host material is taken to be homogeneous). The Born approximation assumes that the flaw is sufficiently similar to the surrounding host material that the fields appearing in Eq. (10.64) can be replaced approximately by those of the known incident wave. Physically, this means that to first order we are assuming that the incident wave passes through the flaw undisturbed, as shown in Fig. 10.38. For a pulse-echo setup and a homogeneous, isotropic flaw in a homogeneous, isotropic medium, for example, this results in a scattering amplitude expression given by [Fundamentals]

$$A\left(\mathbf{e}_i^\beta;-\mathbf{e}_i^\beta\right)=\frac{-\omega^2}{2\pi c_\beta^2}\left[\frac{\Delta\rho}{\rho}+\frac{\Delta c_\beta}{c_\beta}\right]\int_{V_f}\exp\left(2ik_\beta\mathbf{x}\cdot\mathbf{e}_i^\beta\right)dV\left(\mathbf{x}\right) \qquad (10.65)$$

that can, like the Kirchhoff approximation, be analytically evaluated for some simple flaw shapes. A similar expression can also be obtained for more general pitch-catch setups [Fundamentals]. An important feature of Eq. (10.65) is that the material properties of the flaw (contained in the coefficient of the integral) are completely separated from the flaw geometry information (contained in the integral itself). This separation has allowed the Born approximation to be successfully used in a number of flaw sizing applications [Fundamentals]. For a spherical inclusion Eq. (10.65) gives [Fundamentals]

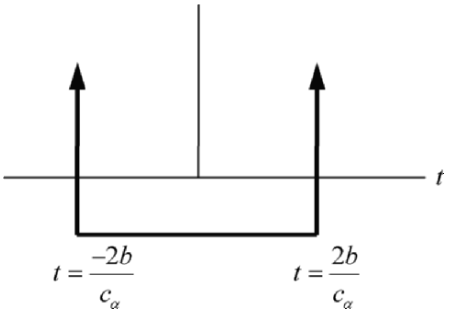

Fig. 10.39. The impulse response for the pulse echo scattering of a spherical inclusion of radius b in the Born approximation. The time $t = 0$ is when the incident wave front reaches the center of the flaw.

$$A\left(\mathbf{e}_i^{\beta};-\mathbf{e}_i^{\beta}\right)=-b\left[\frac{\Delta\rho}{\rho}+\frac{\Delta c_{\beta}}{c_{\beta}}\right]\left[\frac{\sin\left(2k_{\beta}b\right)-2k_{\beta}b\cos\left(2k_{\beta}b\right)}{2k_{\beta}b}\right], \tag{10.66}$$

which can also be written in the alternate form

$$A\left(\mathbf{e}_i^{\beta};-\mathbf{e}_i^{\beta}\right)=-4k_{\beta}^2b^3F\frac{j_1\left(2k_{\beta}b\right)}{2k_{\beta}b}, \tag{10.67}$$

where j_1 is a spherical Bessel function of order one and

$$F=\frac{1}{2}\left(\frac{\Delta\rho}{\rho}+\frac{\Delta c}{c_{\beta}}\right). \tag{10.68}$$

If one inverts either Eq. (10.66) or (10.67) into the time domain, the impulse response of the spherical inclusion is the wave form shown in Fig. 10.39 [Fundamentals]. Like the Kirchhoff approximation, the Born approximation predicts a leading edge delta function response. This delta function is followed by a constant response as the wave passes through the entire flaw, and then one sees a trailing edge delta function response (which is equal to the leading edge delta function response) at the time when the wave has just finished passing through the flaw. Like the Kirchhoff approximation, the Born approximation is a single interaction type of approximation so that it neglects any other wave-flaw interactions such as creeping waves, multiple internal reflections, etc. Like the Kirchhoff approximation the Born approximation can also be applied to

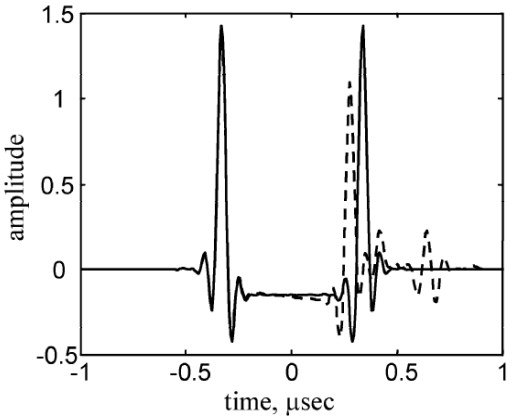

Fig. 10.40. The time domain pulse-echo P-wave response of a 1 mm radius spherical inclusion in steel where the density and compressional wave speed are both ten percent higher than the host steel. Solid line: Born approximation, dashed line: separation of variables solution.

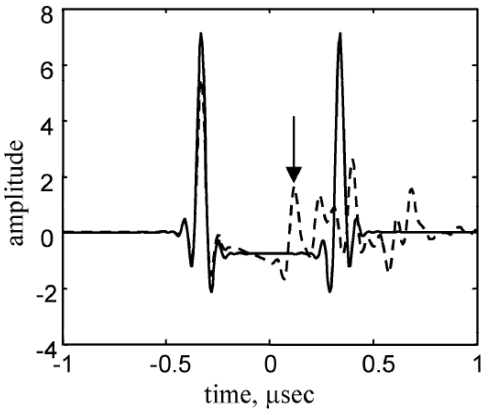

Fig. 10.41. The time domain pulse-echo P-wave response of a 1 mm radius spherical inclusion in steel where the density and compressional wave speed are both fifty percent higher than the host steel. Solid line: Born approximation, dashed line: separation of variables solution.

complex shaped flaws by performing the necessary integrations numerically.

Since the method of separation of variables can be used to obtain the "exact" solution for spherical inclusions, we can use that method to examine the accuracy of the wave form predictions of the Born approximation, just as we did with the Kirchhoff approximation for the spherical void (see Fig. 10.10). In the void case we used the separation of variables method to calculate the response to a relatively high frequency and then subtracted out (in the frequency domain) the known leading edge delta function response before inverting the result into the time domain with an FFT. Since the high frequency content of the other wave contributions (remainder of the lit surface response, creeping wave, etc.) is very small in pulse-echo for P-waves incident on a spherical void, we get in effect an infinite bandwidth time-domain response when we simply add the delta function back into the wave form symbolically, as done in Fig. 10.10. For weak-scattering inclusions the same process is not possible since the front and back surfaces are both delta functions. In the Born approximation these delta functions are always of equal amplitude but in comparing the Born approximation with the method of separation of variables it is found that the back surface delta function is only equal in amplitude to the front surface delta function in the very weak scattering limit and for all other flaws the back surface changes amplitude in an unknown fashion. Thus we cannot remove the delta functions from the Born response analytically, but we can still calculate the Born approximation and separation of variables responses over a range of frequencies and smoothly taper the high frequency response to zero with a cosine-squared windowing filter to reduce time domain "ringing". This is the method used here to compare the Born and separation of variables solutions in the following discussions. In all cases the cosine-squared filter began with values of one at 10 MHz and ended with a zero value at 20 MHz.

Figure 10.40 shows the pulse-echo P-wave response calculated in this fashion for a 1 mm radius spherical inclusion in steel where both the density and compressional wave speed of the inclusion was taken to be ten percent higher than the host steel. It can be seen for even these relatively small material changes the Born approximation does not accurately represent both the amplitude and time of arrival of the back surface response and there are other later arriving waves that are not predicted by the Born approximation. If one examines the same size inclusion in steel but takes the density and compressional wave speed to be 50% higher than the host then as seen in Fig. 10.41 the Born approximation is even more in error, with the back surface response located at a time well removed from

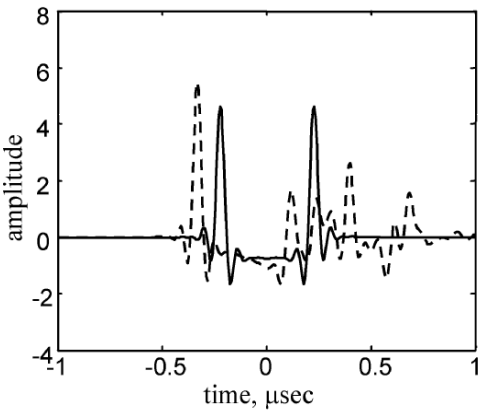

Fig. 10.42. The time domain pulse-echo P-wave response of a 1 mm radius spherical inclusion in steel where the density and compressional wave speed are both fifty percent higher than the host steel. Solid line: Doubly Distorted Born approximation, dashed line: separation of variables solution.

the actual back surface signal (located at the arrow in Fig. 10.41) and even the front surface leading edge response is significantly in error (Note: the specific changes in density and wave speed taken for this case and others that will be considered later are not intended to represent any particular real inclusion but are simply being used here to study the effects of large or small differences between the host and flaw materials). Having the leading edge response amplitude in error is particularly troublesome because it means that the Born approximation could not be reliably used to predict the detectability of inclusions except in the very weak scattering limit, which is not likely to be found in many real tests. A modified ad hoc approximation, called the *doubly distorted Born approximation* (DDBA) [10.12] was recently developed to try to remove some of these deficiencies of the ordinary Born approximation. In the DDBA, it was recognized that the wave field traveling in the flaw does not travel at the wave speed of the host material as assumed in the ordinary Born approximation. Instead, disturbances in the flaw should be traveling at the wave speed of the flaw material. Thus, the wave speeds appearing in both the integral kernel of the Born approximation expression and in the coefficient of that integral were changed in the DDBA from that of the host material to that of the flaw. For the pulse-echo response of a spherical inclusion, this change causes Eq. (10.67) to become instead

$$A\left(\mathbf{e}_i^{\beta};-\mathbf{e}_i^{\beta}\right)_{DDBA}=-4k_{f\beta}^2b^3\tilde{F}\frac{j_1\left(2k_{f\beta}b\right)}{2k_{f\beta}b}, \tag{10.69}$$

where $k_{f\beta}=\omega/c_{f\beta}$ is the wave number based on the flaw wave speed, $c_{f\beta}$, and the function, $\tilde{F}$, is given by

$$\tilde{F}=\frac{1}{2}\left(\frac{\Delta\rho}{\rho_f}+\frac{\Delta c}{c_{f\beta}}\right). \tag{10.70}$$

Figure 10.42 shows the result of using the DDBA on the same case shown in Fig. 10.40 (the pulse-echo P-wave response of a 1 mm radius inclusion in steel where the density and compressional wave speed are 50% higher than the host). Comparing the DDBA results of Fig. 10.42 with the Born approximation results of Fig. 10.41, we see that the DDBA amplitude of the leading edge response is closer to the separation of variables result than that of the Born approximation and also the time separation of the front and back surface responses in the DDBA now agrees with the separation of variables solution. However, the time of arrival of the front surface leading edge response is now incorrect, as seen in Fig. 10.41. The improvement in the leading edge response obtained with the DDBA can be understood by examining the behavior of the functions F and $\tilde{F}$. In [Fundamentals] it was noted that in pulse-echo the F function is just the weak scattering limit of the plane wave reflection coefficient, $R_{12}^{\beta;\beta}$ between the host and flaw materials, i.e.

$$\begin{aligned}F&=\frac{1}{2}\left(\frac{\Delta\rho}{\rho}+\frac{\Delta c}{c_\beta}\right)\\&=R_{12}^{\beta;\beta}+O\left(\left(\Delta\rho/\rho\right)^2,\left(\Delta c/c_\beta\right)^2\right)\\&=\frac{\rho_f c_{f\beta}-\rho c_\beta}{\rho_f c_{f\beta}+\rho c_\beta}+O\left(\left(\Delta\rho/\rho\right)^2,\left(\Delta c/c_\beta\right)^2\right).\end{aligned} \tag{10.71}$$

The functions F and $\tilde{F}$ together with $R_{12}^{\beta;\beta}$ are plotted versus $\Delta\rho/\rho=\Delta c/c_\beta=\lambda$ in Fig. 10.43. From that figure, we can see that the $\tilde{F}$ function does a much better job of following the behavior of $R_{12}^{\beta;\beta}$ for even large changes of density and wave speed. Since at high frequencies our previous discussions have shown that the pulse-echo leading edge response

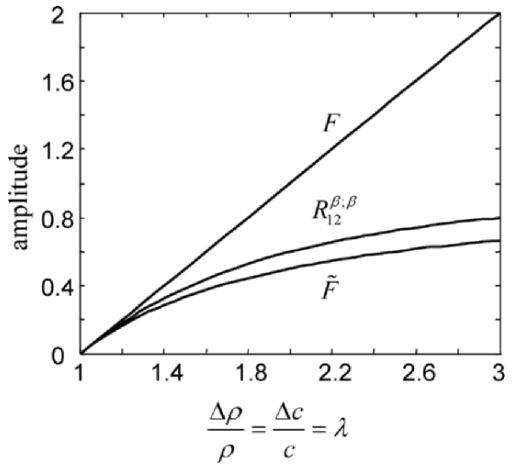

Fig. 10.43. A comparison of the F and $\tilde{F}$ functions and the plane wave reflection coefficient, $R_{12}^{\beta;\beta}$.

is controlled by $R_{12}^{\beta;\beta}$ (see Eq. (10.19)), the closer agreement of $\tilde{F}$ to this reflection coefficient is the reason for the improvements seen in Fig. 10.42. However, this fact also suggests that if one replaces the $\tilde{F}$ function in the DDBA by $R_{12}^{\beta;\beta}$ and includes a phase correction term to the DDBA to fix up its incorrect arrival time for the leading edge response, one should have a new model that agrees better with the separation of variables result. This new model we will call the *modified Born approximation* (MBA) [10.13]. In the MBA model Eq. (10.69) becomes

$$A\left(\mathbf{e}_i^{\beta};-\mathbf{e}_i^{\beta}\right)_{MBA} = -4k_{f\beta}^2 b^3 R_{12}^{\beta;\beta} \exp\left[2ik_{f\beta}b\left(1-c_{f\beta}/c_{\beta}\right)\right] \cdot \frac{j_1\left(2k_{f\beta}b\right)}{2k_{f\beta}b}. \tag{10.72}$$

Figure 10.44 shows the result of using the MBA model on the same case shown in Figs. 10.41 and 10.42 (the pulse-echo P-wave response of a 1 mm radius inclusion in steel where the flaw density and compressional wave speed are 50% higher than the host). It can be seen that the leading edge amplitude and time of arrival are now both correct as is the time of arrival of the back surface response. The MBA model will still model the amplitude of the back surface response as equal to the front surface amplitude and will not contain any of the other responses seen in the

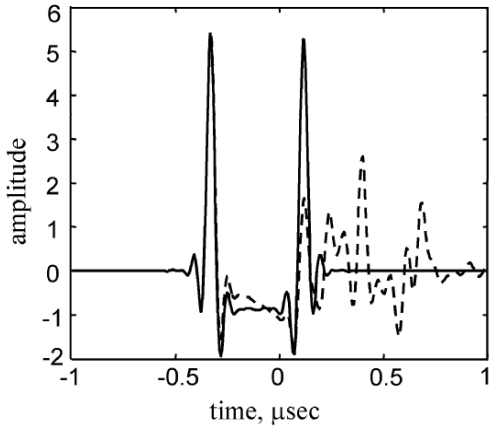

Fig. 10.44. The time domain pulse-echo P-wave response of a 1 mm radius spherical inclusion in steel where the density and compressional wave speed are both fifty percent higher than the host steel. Solid line: MBA model, dashed line: separation of variables solution.

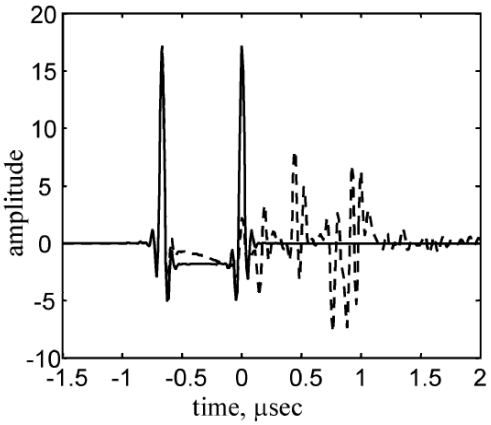

Fig. 10.45. The time domain pulse-echo P-wave response of a 1 mm radius spherical inclusion in steel where the density and compressional wave speed are both one hundred percent higher than the host steel. Solid line: MBA model, dashed line: separation of variables solution.

separation of variables solution, but in general Eq. (10.72) gives much better results than either the original Born or the DDBA models. Like the DDBA the MBA model is an ad hoc modification of the Born approximation but it appears to be a useful modification for dealing with inclusions that may be far from being weak scatterers. This can be seen in Figure 10.45 where the pulse-echo P-wave response for a 1 mm radius inclusion in steel is shown for a case with the flaw density and wave speed both 100% higher than that of the host material. Even in this extreme case the MBA model continues to capture the leading edge response correctly. For the pulse-echo response of a more general shaped inclusion, the MBA gives, from Eq. (10.65)

$$A\left(\mathbf{e}_i^{\beta};-\mathbf{e}_i^{\beta}\right)_{MBA}=\frac{-\omega^2}{\pi c_{f\beta}^2}R_{12}^{\beta;\beta}\exp\left[2ik_{f\beta}r_e\left(1-c_{f\beta}/c_{\beta}\right)\right]\cdot\int_{V_f}\exp\left(2ik_{f\beta}\mathbf{x}\cdot\mathbf{e}_i^{\beta}\right)dV\left(\mathbf{x}\right) \tag{10.73}$$

where r_e is the distance in the incident wave direction from a fixed point (usually the "center" of the flaw) to the point on the flaw surface where the incident wave front first touches the flaw.

One could of course use Eq. (10.19) to model just the leading edge response of an inclusion, even for more general pitch-catch setups. The advantage of using Eq. (10.73) is that although it is only valid for pulse-echo inspections it also captures the main features of the entire flaw response correctly in the weak scattering limit.

10.8 Separation of Variables Solutions

For spherical or cylindrical shaped scatterers in an elastic solid, one can use the method of separation of variables to express the exact scattering solution as an infinite sum of spherical Hankel functions and associated Legendre functions for the case of the sphere, and Hankel functions and complex exponential functions for the cylinder [10.14 – 10.25]. Even though both geometries are very simple shapes, they are useful for considering important scatterers such as pores or a side-drilled hole and they can serve as reference solutions for testing the accuracy of approximate methods. Although the separation of variables solutions are exact, they are expressed in terms of infinite sums that must be calculated numerically and more terms are needed as the scatterer becomes larger or the frequency becomes higher. Normally this is not a problem since with modern PCs

it is possible to calculate scattering results for non-dimensional frequencies as high as, say, $kb \cong 100$.

In this section we will give the separation of variables solution for four cases: the pulse-echo response of a spherical void for both P-waves and S-waves, and the pulse echo response of a cylindrical void for P-waves and S-waves. These solutions have also been coded in MATLAB functions which are given in Appendix G.

First, consider the case of the pulse-echo P-wave response of a spherical void of radius *b*. Using the method of separation of variables, we find that [10.14], [Fundamentals]

$$A\left(\mathbf{e}_i^p;-\mathbf{e}_i^p\right)=\frac{-1}{ik_p}\sum_{n=0}^{\infty}(-1)^n\,A_n, \tag{10.74}$$

where

$$A_n=\frac{E_3E_{42}-E_4E_{32}}{E_{31}E_{42}-E_{41}E_{32}} \tag{10.75}$$

and we have

$$\begin{aligned}
E_3&=(2n+1)\left\{\left[n^2-n-\left(k_s^2b^2/2\right)\right]j_n\left(k_{pb}\right)+2k_pbj_{n+1}\left(k_pb\right)\right\}\\
E_4&=(2n+1)\left\{(n-1)\,j_n\left(k_{pb}\right)-k_pbj_{n+1}\left(k_pb\right)\right\}\\
E_{31}&=\left[n^2-n-\left(k_s^2b^2/2\right)\right]h_n^{(1)}\left(k_pb\right)+2k_pbh_{n+1}^{(1)}\left(k_pb\right)\\
E_{41}&=(n-1)h_n^{(1)}\left(k_pb\right)-k_pbh_{n+1}^{(1)}\left(k_pb\right)\\
E_{32}&=-n(n+1)\left[(n-1)h_n^{(1)}\left(k_sb\right)-k_sbh_{n+1}^{(1)}\left(k_sb\right)\right]\\
E_{42}&=-\left[n^2-1-\left(k_s^2b^2/2\right)\right]h_n^{(1)}\left(k_sb\right)-k_sbh_{n+1}^{(1)}\left(k_sb\right).
\end{aligned} \tag{10.76}$$

For the SV-wave case, the separation of variables solution is of the form [10.18]

$$A\left(\mathbf{e}_i^s;-\mathbf{e}_i^s\right)=\frac{-1}{ik_s}\sum_{n=1}^{\infty}\frac{(-1)^n(2n+1)B_n}{2}, \tag{10.77}$$

where

$$B_n=\frac{H_{13}J_{42}-H_{43}J_{12}}{H_{13}H_{42}-H_{43}H_{12}}-\frac{J_{41}}{H_{41}} \tag{10.78}$$

and

$$
\begin{aligned}
J_{12} &= n(n+1)\left[(n-1)\, j_n(k_s b) - k_s b\, j_{n+1}(k_s b)\right] \\
H_{12} &= n(n+1)\left[(n-1) h_n^{(1)}(k_s b) - k_s b\, h_{n+1}^{(1)}(k_s b)\right] \\
H_{13} &= \left[n^2 - n - \left(k_s^2 b^2/2\right)\right] h_n^{(1)}(k_p b) + 2k_p b\, h_{n+1}^{(1)}(k_p b) \\
J_{41} &= (n-1)\, j_n(k_s b) - k_s b\, j_{n+1}(k_s b) \\
H_{41} &= (n-1) h_n^{(1)}(k_s b) - k_s b\, h_{n+1}^{(1)}(k_s b) \\
J_{42} &= \left[n^2 - 1 - \left(k_s^2 b^2/2\right)\right] j_n(k_s b) + k_s b\, j_{n+1}(k_s b) \\
H_{42} &= \left[n^2 - 1 - \left(k_s^2 b^2/2\right)\right] h_n^{(1)}(k_s b) + k_s b\, h_{n+1}^{(1)}(k_s b) \\
H_{43} &= (n-1) h_n^{(1)}(k_p b) - k_p b\, h_{n+1}^{(1)}(k_p b).
\end{aligned}
\tag{10.79}
$$

The pulse-echo P-wave time-domain response for a spherical void was shown previously in Fig. 10.10. There we could simply subtract off the leading edge response from the separation of variables solution in the frequency domain and then apply the inverse Fourier transform to the remaining portion of the response, which contains only low frequency signals. However, for the pulse-echo SV-wave response, the creeping waves are more significant and extend to very high frequencies. Figure 10.46 shows the magnitude of the pulse-echo SV-wave scattering amplitude of a 0.5 mm radius spherical pore in steel. The deep oscillations in the SV-wave response at high frequencies in comparison with the highly damped oscillations appearing in Fig. 10.8 for the P-wave response shows that a simple subtraction of the leading edge response will not lead to a response confined only to low frequencies. However, we can follow the procedure used in the Born approximation and apply a cosine-squared windowing filter to the frequency domain scattering amplitude before inverting the signal back into the time domain. Figure 10.47 shows the resulting time-domain SV-wave signal for the 0.5 mm radius pore in steel. For comparison purposes Fig. 10.48 shows the time-domain pulse-echo P-wave response for the 0.5 mm radius spherical pore in steel as calculated with the same filter function used in the Born approximation studies. It can be seen while the leading edge responses are almost identical in the two cases that the creeping wave in the P-wave case is indeed much smaller than in the SV-wave case.

For the case of a cylindrical void of radius *b* with the incident wave direction in a plane perpendicular to the axis of the cylinder, the 2-D separation of variables solution can be used to generate a normalized 3-D

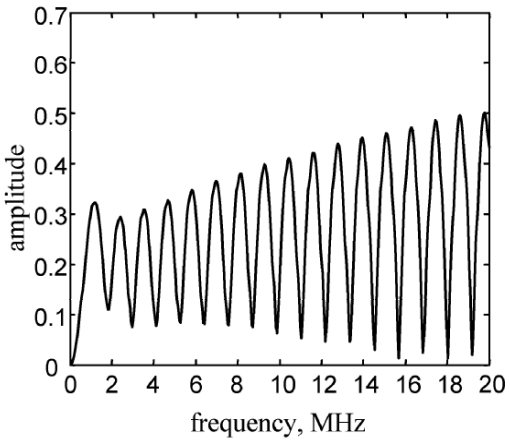

Fig. 10.46. The magnitude of the pulse-echo SV-wave response, $A(\mathbf{e}_i;-\mathbf{e}_i)$, versus frequency for a 0.5 mm radius spherical void in steel ($c_p = 5900$ m/s, $c_s = 3200$ m/sec) as calculated by the method of separation of variables.

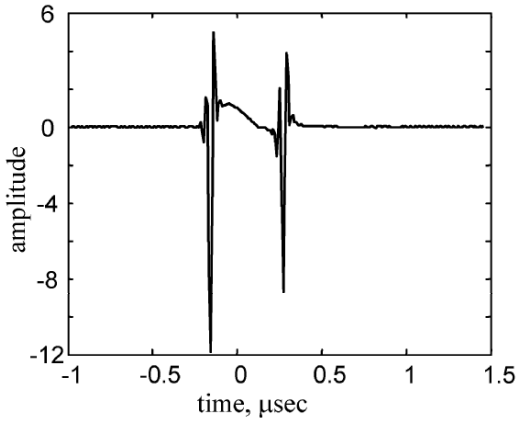

Fig. 10.47. The time domain response corresponding to Fig. 10.46 by applying a low-pass cosine-squared windowing filter between 10 and 20 MHz to the separation of variables solution and then inverting the result into the time domain with the inverse Fourier transform.

scattering amplitude for a cylinder of length L, as discussed previously. For an incident P-wave

$$\frac{A_{3D}\left(\mathbf{e}_i^p;-\mathbf{e}_i^p\right)}{L}=\frac{i}{2\pi}\sum_{n=0}^{\infty}\left(2-\delta_{0n}\right)\left(-1\right)^n F_n, \tag{10.80}$$

where

$$\delta_{0n}=\begin{cases}1 & n=0\\ 0 & otherwise\end{cases} \tag{10.81}$$

and

$$F_n=1+\frac{C_n^{(2)}\left(k_pb\right)C_n^{(1)}\left(k_sb\right)-D_n^{(2)}\left(k_pb\right)D_n^{(1)}\left(k_sb\right)}{C_n^{(1)}\left(k_pb\right)C_n^{(1)}\left(k_sb\right)-D_n^{(1)}\left(k_pb\right)D_n^{(1)}\left(k_sb\right)} \tag{10.82}$$

with

$$\begin{aligned}C_n^{(i)}\left(x\right)&=\left(n^2+n-\left(k_sb\right)^2/2\right)H_n^{(i)}\left(x\right)-\left(2nH_n^{(i)}\left(x\right)-xH_{n+1}^{(i)}\left(x\right)\right)\\ D_n^{(i)}\left(x\right)&=n\left(n+1\right)H_n^{(i)}\left(x\right)-n\left(2nH_n^{(i)}\left(x\right)-xH_{n+1}^{(i)}\left(x\right)\right)\end{aligned} \tag{10.83}$$

for $\left(i=1,2\right)$.

For S-waves, the polarization vector of the incident wave is assumed to lie in the plane perpendicular to the axis of the cylinder, so if we let that axis be horizontal, we are considering vertically polarized S-waves, i.e. SV-waves. Note that the 2-D scattering problem for horizontally polarized shear (SH) waves is just equivalent to a purely scalar scattering problem with no mode conversion while the SV-case does involve a coupling between P-waves and SV-waves. Here, we will only consider the SV-wave case as that is the one most commonly encountered in NDE setups. Again, transforming the 2-D separation of variables solution to a normalized 3-D scattering amplitude we have

$$\frac{A_{3D}\left(\mathbf{e}_i^{sv};-\mathbf{e}_i^{sv}\right)}{L}=\frac{i}{2\pi}\sum_{n=0}^{\infty}\left(2-\delta_{0n}\right)\left(-1\right)^n G_n \tag{10.84}$$

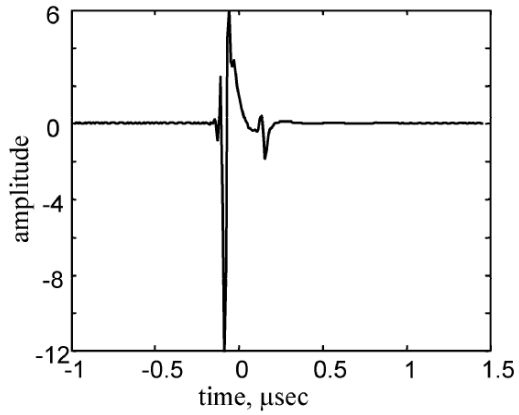

Fig. 10.48. The time-domain pulse-echo P-wave response of a 0.5 mm radius spherical void in steel ($c_p = 5900$ m/s, $c_s = 3200$ m/sec) obtained by applying a low-pass cosine-squared windowing filter between 10 and 20 MHz to the separation of variables solution and then inverting the result into the time domain with the inverse Fourier transform.

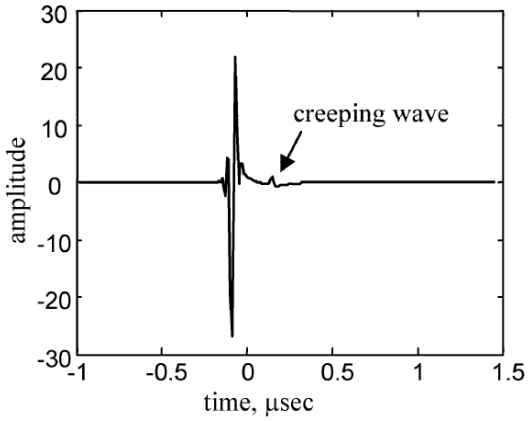

Fig. 10.49. The time-domain pulse-echo P-wave response of a 0.5 mm radius cylindrical void in steel ($c_p = 5900$ m/s, $c_s = 3200$ m/sec) obtained by applying a low-pass cosine-squared windowing filter between 10 and 20 MHz to the separation of variables solution and then inverting the result into the time domain with the inverse Fourier transform.

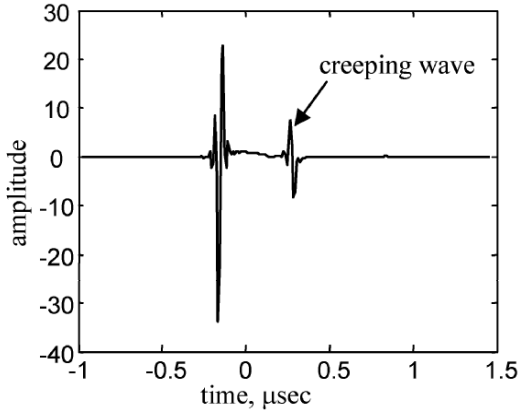

Fig. 10.50. The time-domain pulse-echo SV-wave response of a 0.5 mm radius cylindrical void in steel ($c_p = 5900$ m/s, $c_s = 3200$ m/sec) obtained by applying a low-pass cosine-squared windowing filter between 10 and 20 MHz to the separation of variables solution and then inverting the result into the time domain with the inverse Fourier transform.

where

$$G_n = 1 + \frac{C_n^{(2)}(k_s b)\, C_n^{(1)}(k_p b) - D_n^{(2)}(k_s b)\, D_n^{(1)}(k_p b)}{C_n^{(1)}(k_p b)\, C_n^{(1)}(k_s b) - D_n^{(1)}(k_p b)\, D_n^{(1)}(k_s b)}. \tag{10.85}$$

These solutions were used in Figs. 10.33-36 to calculate the "exact" solutions that were compared with the Kirchhoff approximation in the frequency domain. We can calculate these pulse-echo separation of variables solutions and then use a cosine-squared window again, as done for the spherical void, that allows us to invert these frequency domain values back into the time domain. The results for the P-wave response of a 0.5 mm radius cylindrical void in steel are shown in Fig. 10.49, and the corresponding SV-wave response is shown in Fig. 10.50. It can be seen that the creeping wave in the P-wave case is very small while it is much larger in the SV-wave case. In both cases, the early time response of the cylinder (Note: this early time response is not the leading edge response calculated earlier for 3-D scatterers), which is predicted well by the Kirchhoff approximation, is the dominant part of the overall pulse-echo response, which demonstrates that the Kirchhoff approximation works well

except for very small flaws where the creeping wave and early time responses merge.

10.9 Other Scattering Models and Methods

In addition to the Born and Kirchhoff approximations there are other approximate methods that have been used to model flaw scattering problems, including elastodynamic ray theory (used to model the scattering of cracks) [10.26], [10.27] and approximate low frequency expansions [10.28 -10.30]. The high frequency ray methods lead to rather complex expressions and in certain cases singularities appear that invalidate the approximation. Low frequency expansions can produce some explicit analytical results but these have been of limited use in NDE applications because the responses of flaws of interest often are well beyond the range where such expansions are valid. This is unfortunate since it has been shown that there is much useful information in the low frequency response of flaws [10.30].

Besides the method of separation of variables there are five other numerical methods that have been commonly used for solving flaw scattering problems: the T-matrix method or the closely related method of optimal truncation (MOOT), the method of finite differences, the finite element method, the boundary element method, and the elastodynamic finite integration technique (EFIT).

The T-matrix method and the method of optimal truncation (MOOT) express the scattering solution for shapes other than spheres and cylinders in terms of the same special functions used in the method of separation of variables [10.31-10.35]. These two methods differ only in the way they approximately satisfy the boundary conditions. Both spheroidal and circular crack-like geometries have been considered with these methods. Like the separation of variables methods, these solutions are expressed in terms of infinite series and it is necessary to keep a sufficiently large number of terms in order to guarantee convergence of the solutions.

The method of finite differences has also been applied to flaw scattering problems [10.36], [10.37]. Unlike the separation of variables or T-matrix methods, this approach approximates the governing differential equations of motion directly in the time domain for the elastic material surrounding the flaw and replaces those equations with corresponding difference equations which are then solved numerically for field values defined on a mesh (or “grid”) of discrete points as a function of time. This

method can in principle handle rather general problems but in practice there are a number of issues that have limited the use of this method. First, it is convenient to use regular shaped meshes (such as rectangular meshes) with this method, but such meshes do not readily allow one to satisfy the boundary conditions at the flaw surface if that surface is rather complex. Second, since all of the material exterior to the flaw must be meshed, to keep the computational burden manageable the mesh must eventually be artificially truncated, leading to "fictitious" boundaries. Extraneous waves are generated at such fictitious boundaries that must be suppressed. This is often done by the application of special absorbing boundary conditions at the fictitious boundaries that minimize the extra waves generated or by keeping the fictitious surfaces sufficiently far from the flaw so that the extraneous waves do not contaminate the solution for the time interval considered. Finally, another problem inherent to the finite difference method is the large amount of computations needed, particularly for 3-D scattering problems. Thus even on modern computers, many of the finite difference solutions one sees are for 2-D problems. One nice feature of this method, however, is that it yields the solutions at all points in the solid directly, which allows one to view the complex wave/flaw interactions present in graphical form, including movies of those interactions. The mass-spring lattice model of Yim is a recent model of the finite difference type that has been used in this manner [10.38].

The finite element method, like the finite difference method, solves for the scattered fields on a mesh of discrete points [10.39], [10.40]. In the finite element method, however, the mesh is generated by an assemblage of small elements which can have different shapes so that it is not difficult to adapt the mesh to even complicated flaw shapes. Unlike the finite difference method, however, the finite element method does not directly approximate the equations of motion but instead it minimizes an energy functional for the assemblage of elements where the fields and material properties in each element are approximated by relatively simple functions such as polynomials. This allows the finite element method to model very complex materials, including both inhomogeneous and anisotropic materials. Ultimately, the finite element method generates a large, banded system of simultaneous equations that must be solved numerically. Like the finite difference method, the finite element method must deal with fictitious boundaries and suppress the extra waves generated by those boundaries. Perhaps the greatest challenge faced with the finite element method is the "curse of small wavelength", i.e. in order to maintain accurate solutions the finite element method must keep the element size very small (on the order of 5-10 elements per wavelength). Since most NDE applications use very high frequency waves (and hence

the corresponding wavelengths are very small) this limitation makes it very computationally intensive to simulate general 3-D problems, so that (like with finite differences) one often sees finite element solutions applied to simpler 2-D or axisymmetric situations.

The boundary element method is an attractive method for solving flaw scattering problems [10.41-10.45] since it uses a fundamental solution for waves in the solid to generate integral equations for the displacements and tractions on the flaw surface, and these are precisely the fields needed to calculate the scattered waves and the far-field scattering amplitude of the flaw. These integral equations are solved by breaking the flaw surface into small elements and assuming some simple form for the fields in each element, which leads to a large set of simultaneous equations. Unlike the finite element system, however, the boundary element system of equations is not banded. Because the boundary element method deals only with the fields on the surface of the flaw, there are no fictitious surfaces in the solid that need to be considered with this method. In fact, the boundary element method can easily handle flaw scattering problems in infinite regions. However, when dealing with volumetric flaws the boundary element solution can be contaminated by fictitious resonances that render the solution inaccurate at certain frequencies so that special procedures need to be taken to suppress this unwanted behavior. Like the finite element method the boundary element method is affected by the curse of small wavelength. Thus, it is generally very computationally expensive in terms of both computer storage and calculation time to consider 3-D scattering problems with the boundary element method for, say, $kb > 20$. Perhaps the most important limitation of this method is the need for a fundamental solution to generate the requisite integral equations. Although a fundamental solution for a homogeneous, isotropic solid is available in exact analytical form [Fundamentals], for homogeneous anisotropic materials the fundamental solution is only known in an integral form that must be calculated numerically [10.46] and such fundamental solutions are not available for general inhomogeneous materials.

The elastodynamic finite integration technique (EFIT) is similar in some respects to the finite difference method in that it works with an approximation of the equations of motion, but, unlike the finite difference method, EFIT uses an integral form of those equations of motion [10.47]. Like the finite difference and finite element methods, EFIT can serve as both a beam model and a flaw scattering model since both of those aspects of the wave-flaw interactions are treated simultaneously. Also, like the other numerical methods, the generality of the EFIT approach, which in principle can handle quite complex inhomogeneous and anisotropic media problems, has to be weighed against its overall numerical costs.

There is still considerable opportunity for improving the state of the art in flaw scattering modeling for NDE applications. Although approximate methods such as the Kirchhoff and Born approximation are very valuable, they are limited in the features of the scattering process that they can simulate, while more exact numerical methods suffer from computational inefficiencies. Surface breaking cracks, porosity, and multiple distributed cracks (as found in stress-corrosion cracking problems), are examples where simple, efficient, and accurate scattering models are not currently available.

10.10 References

10.1 Schmerr LW, Sedov A (2003) Modeling ultrasonic problems for the 2002 benchmark session. In: Thompson DO, Chimenti DE (eds) Review of progress in quantitative nondestructive evaluation 22B. American Institute of Physics, Melville, NY, pp 1776-1783

10.2 Harker AH (1988) Elastic waves in solids. Institute of Physics Publishing Ltd., Bristol, England

10.3 Charlesworth JP, Temple JAG (2001) Engineering applications of ultrasonic time-of-flight diffraction. Research Studies Press, Philadelphia, PA

10.4 Gradshteyn IS, Ryzhik IM (1980) Table of integrals, series, and products. Academic Press, New York, NY

10.5 Abramowitz M, Stegun IA (1965) Handbook of mathematical functions. Dover Publications, New York, NY

10.6 Brind RJ, Achenbach JD, Gubernatis JE (1984) High-frequency scattering of elastic waves from cylindrical cavities. Wave Motion 6: 41-60

10.7 Gubernatis JE, Domany E , Krumhansl JA, Hubermann M (1977) The Born approximation in the theory of scattering of elastic waves by flaws. J. Appl. Phys. 48: 2812-2819

10.8 Hudson JA, Heritage JR (1981) The use of the Born approximation in seismic scattering problems. Geophys. J. Royal Astron. Soc. 66: 221-240

10.9 Gubernatis JE, Domany E , Krumhansl JA (1977) Formal aspects of the theory of scattering of ultrasound by flaws in elastic materials. J. Appl. Phys. 48: 2804-2811

10.10 Rose JH, Richardson JM (1982) Time domain Born approximation. Journ. Nondestr. Eval. 3: 45-53

10.11 Rose JH (1989) Elastic wave inverse scattering in nondestructive evaluation. Pure Appl. Geophys. 131: 715-739

10.12 Darmon M, Calmon P, Bele B (2004) An integrated model to simulate the scattering of ultrasound by inclusions in steels. Ultrasonics 42: 237-241

10.13 Huang R, Schmerr LW, Sedov A (2006) A modified Born approximation for scattering in isotopic and anisotropic elastic solids. Journ. Nondestr. Eval. 25: 139-154

10.14 Ying CF, Truell R (1956) Scattering of a plane compressional wave by a spherical obstacle in an isotropically elastic solid. J. Appl. Phys. 27: 1086-1097
10.15 Pao YH, Mow CC (1963) Scattering of a plane compressional wave by a spherical obstacle. J. Appl. Phys. 34: 493-499
10.16 Varadan VV, Ma Y, Varadan VK, Lakhtakia A (1991) Scattering of Waves by Spheres and Cylinders. In: Varadan VV, Lakhtakia A, Varadan VK (eds) Field representations and introduction to scattering. Elsevier Science publishers, Amsterdam, The Netherlands, Chapter 5
10.17 Pao YH, Mow CC (1973) Diffraction of elastic waves and dynamic stress concentrations. Crane, Russak and Co., New York, NY
10.18 Einspruch N, Witterholt E, Truell R (1960) Scattering of a plane transverse wave by a spherical obstacle in an elastic medium. J. Appl. Phys. 31: 806-818
10.19 McBride RJ, Kraft DW (1972) Scattering of a transverse elastic wave by an elastic sphere in a solid medium. J. Appl. Phys. 43: 4853-4861
10.20 Knopoff L (1959) Scattering of shear waves by spherical obstacles. Geophysics 24: 209-219
10.21 Morse PM, Feshbach H (1953) Methods of theoretical physics, parts I and II. McGraw-Hill, New York, NY
10.22 Einspruch N, Truell R (1960) Scattering of a plane longitudinal wave by a spherical fluid obstacle in an elastic medium. J. Acoust. Soc. Am. 32: 214-220
10.23 Truell R, Elbaum C, Chick BB (1969) Ultrasonic methods in solid state physics. Academic Press, New York, NY
10.24 Kraft DW, Franzblau M (1971) Scattering of elastic waves from a spherical cavity in a solid medium. J. Appl. Phys. 42: 3019-3024
10.25 Knopoff L (1959) Scattering of compressional waves by spherical obstacles. Geophysics 24: 30-39
10.26 Achenbach JD, Gautesen AK, McMaken H (1982) Ray methods for waves in elastic solids. Pitman Books Ltd., Boston, MA
10.27 Langenberg KJ, Schmitz V (1986) Numerical modeling of ultrasonic scattering by cracks. Nuclear Eng. and Design 94: 427-445
10.28 Richardson JM (1984) Scattering of elastic waves from symmetric inhomogeneities at low frequencies. Wave Motion 6: 325-336
10.29 Rose JH (1987) Elastodynamic long wavelength phase. Ultrasonics 25: 141-146
10.30 Kohn W, Rice JR (1979) Scattering of long-wavelength elastic waves from localized defects in solids. J. Appl. Phys. 50: 3346
10.31 Varadan VK, Varadan VV (eds.) (1980) Acoustic, electromagnetic and elastic wave scattering – focus on the T-matrix approach. Pergamon Press, New York, NY
10.32 Varatharajulu V, Pao YH (1976) Scattering matrix for elastic wave I. theory. J. Acoust. Soc. Am. 60: 556-566
10.33 Varadan VV (1978) Scattering matrix for elastic waves II. application to elliptical cylinders. J. Acoust. Soc. Am. 63: 1014-1024

10.34 Opsal JL, Visscher WM (1985) Theory of elastic wave scattering: applications of the method of optimal truncation. J. Appl. Phys. 58: 1102-1115
10.35 Visscher WM (1981) Calculation of the scattering of elastic waves from a penny-shaped crack by the method of optimal truncation. Wave Motion 3: 49-69
10.36 Bond LJ, Punjani M, Safari N (1988) Ultrasonic wave propagation and scattering using explicit finite difference methods. In: Blakemore M, Georgiou GA, (eds) Mathematical modelling in nondestructive testing. Clarendon Press, Oxford, England
10.37 Yamawaki H, Saito T (2000) Numerical calculation of ultrasonic propagation with anisotropy. Nondestr. Test. & Eval. Int'l 33: 489-497
10.38 Yim H, Baek E (2002) Two-dimensional numerical modeling and simulation of ultrasonic testing. J. Korean Soc. Nondestr. Test. 22: 649 -658
10.39 Ludwig R, Lord W (1988) A finite-element formulation for the study of ultrasonic NDT systems. IEEE Trans. Ultrason., Ferro., and Freq. Control UFFC-35: 809-820
10.40 Kishore NN, Sridhar I, Iyengar NGR (2000) Finite element modeling of the scattering of ultrasonic waves by isolated flaws. Nondestr. Test. & Eval. Int'l 33: 297-305
10.41 Dominguez J (1994) Boundary elements in dynamics. Elsevier Applied Science, Amsterdam, The Netherlands
10.42 Kitahara M (1985) Boundary integral equation methods in eigenvalue problems in elastodynamics and thin plates. Studies in applied mechanics Vol. 10, Elsevier, Amsterdam, The Netherlands
10.43 Do Rega Silva J (1994) Acoustic and elastic wave scattering using boundary elements. W.I.T. Press, Southhampton, United Kingdom
10.44 Krishnasamy G, Schmerr LW, Rudolphi T J, Rizzo FJ (1990) Hypersingular boundary integral equations: some applications in acoustic and elastic wave scattering. Trans. ASME, J. Appl. Mech 57: 404-414
10.45 Bonnet M (1995) Boundary integral equation methods for solids and fluids. J. Wiley and Sons, New York, NY
10.46 Wang CY, Achenbach JD (1995) Three-dimensional time-harmonic elasto-dynamic Green's functions for anisotropic solids. Proc. Roy. Soc. London, Ser. A 449: 441-458
10.47 Fellinger P, Marklein R, Langenberg KJ, Klaholz S (1995) Numerical modeling of elastic wave propagation and scattering with EFIT – elastodynamic finite integration technique. Wave Motion 21: 47-66

10.11 Exercises

1. Equations (10.14) and (10.36) give pulse-echo far-field scattering amplitude component versus frequency for a spherical pore and a circular crack, respectively, in the Kirchhoff approximation. In Chapter 12 a

MATLAB function A_void is given that implements Eq. (10.14). The function A_void has as its argument a setup structure that contains all the necessary parameters for ultrasonic flaw response simulations. Rewrite that function as a new MATLAB function, A_pore, that requires only the parameters needed to calculate the scattering amplitude and returns this scattering amplitude with the function call:

```
>> A = A_pore(f, b, c);
```

where f contains the frequencies (in MHz) at which the scattering amplitude is to be evaluated, b is the pore radius (in mm), and c is the wave speed of the surrounding material (in m/sec). By similarly modifying the function A_crack given in Chapter 12, write a new MATLAB function, A_circ, for the pulse-echo response of a circular crack of radius b which has a calling sequence:

```
>> A = A_circ(f, theta, b, c);
```

where theta is the angle (in degrees) that the incident wave makes with the normal to the crack.

In MATLAB generate a vector of 200 frequency values ranging from 0 to 30 MHz and using these two MATLAB functions plot the magnitude of the P-wave pulse-echo scattering amplitude component versus frequency for a 1mm radius pore in steel (c = 5900 m/sec) and a 1 mm radius crack in steel at an incident angle of 10 degrees. Compare your plots to Figs. (10.8) and (10.17).

2. The time-domain pulse-echo scattering amplitude responses of a spherical pore and a circular crack in the Kirchhoff approximation were given by Eqs. (10.15) and (10.39), respectively. These time-domain signals were computed by performing the inverse Fourier transforms of Eqs. (10.14) and (10.36) exactly so that they are for an infinite bandwidth system. Here we want to examine these time-domain responses for finite bandwidths.

(a) In MATLAB generate a vector, f, of 1024 frequencies ranging from 0 to 100 MHz using the function s_space (see Appendix G). Compute the scattering amplitude components of a spherical pore and circular crack for the parameters given in the previous exercise. Multiply these scattering amplitudes (element by element) with the output of the MATLAB function system_f(f, amp, fc, bw) which generates a Gaussian-shaped window of amplitude amp, centered at a frequency, fc, and having a 6 dB bandwidth, bw. Take amp = 1.0, fc = 5.0, bw = 4.0 (see Appendix G). Invert these

products into the time domain using IFourierT and plot the time domain signal versus the time, t. These results show the flaw response as would be typically measured in a relatively wideband ultrasonic system.

(b) Repeat part (a) but replace the function system_f by the function lp_filter (f, fstart, f, end) which is a low-pass filter that is unity for frequencies below fstart and is tapered smoothly to zero at the frequency fend (see Appendix G). For frequencies above fend the filter is zero. Use this function with fstart = 20 MHz, fend = 30 MHz to generate and plot the same time-domain signals found in part (a). Comparing these results with part (a), what can you conclude?